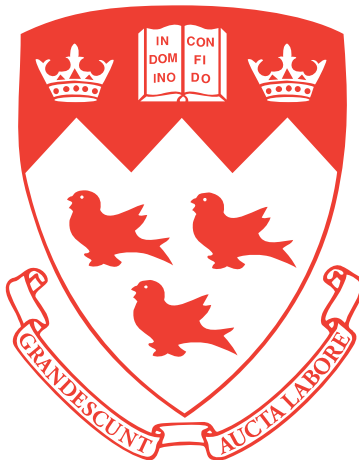


Simulating a One-Dimensional Gas with Suspended Magnets

An Honours Mechanical Engineering Thesis

John Lian



Supervised by

Andrew Higgins

Department of Mechanical Engineering

McGill University

December 2014

Acknowledgements

I would like to thank Professor Andrew Higgins for advising and support. I must also thank all SWPG members: Jason Loiseau, Justin Huneault, William Georges, Myles Hildebrand, and Xiaocheng Mi for their help.

Thanks to Douglas Prisnie for the hard work during the summer. Thanks to all friends and family who supported me during my research.

Lastly I would like to thank Krishna Kumar for developing the template used in this dissertation.

Abstract

A one-dimensional chain of air-bearing-suspended magnets has been constructed to study wave propagation in different media. The air bearing system is demonstrated to be effective in reducing dissipation losses and improving simulation validity. MATLAB programs were developed to reliably track particles from video footage and numerically model particle motion. It is shown that the system investigated can be used to demonstrate wave propagation in both discrete nonlinear and continuous media.

Une chaîne unidimensionnelle d'aimants suspendus par un coussin d'air a été construite pour étudier la propagation des ondes dans différents milieux. Le coussin d'air permet de réduire la friction entre les aimants et le guide, ce qui améliore la validité des simulations. Un code MATLAB a été développé afin de reproduire le trajet des aimants à partir de vidéos des expériences, permettant de créer un modèle numérique qui reproduit le mouvement des aimants. Il est démontré que le système d'aimants peut être utilisé afin d'étudier la propagation des ondes dans les milieux non linéaires, discrets et continus.

Table of Contents

List of Figures	ix
List of Tables	xi
1 Introduction	1
1.1 Different Regimes of Particular Interaction	1
1.1.1 Pulse Velocity for Beads-on-a-Wire	4
1.1.2 Pulse Velocity in Nonlinear Chains	4
1.1.3 Pulse Velocity in a Continuous Spring	5
1.2 Concept	6
1.3 Outline	7
2 Experimental Apparatus	9
2.1 Definition	9
2.2 Previous Design	11
2.3 Challenges and Focus	11
2.4 Magnets and Rod	12
2.4.1 The 6 mm Acrylic Rod	13
2.5 Air Bearing System	15

Table of Contents

2.5.1	Uniform Flow	17
2.5.2	Second-Generation and Final Design Overview	20
2.6	Lighting and Camera	23
3	Experimental Results	27
3.1	Footage Analysis	28
3.2	Particle Trajectories	32
3.2.1	Shock Wave	32
3.2.2	Acoustic Wave	34
3.2.3	Pre-compression	35
4	Modelling	39
4.1	Numerical Simulation	39
4.1.1	Magnetic Force Potential	41
4.1.2	Numerical Simulation Results	49
4.2	Analytical Continuum Modelling	51
5	Conclusion	55
5.1	Future Work	56
References		59
Appendix A	Raw Data From Static Loading	61

List of Figures

1.1	Coulomb's Law	2
1.2	Hertz Law	3
2.1	Magnets on Rod	10
2.2	Design from Previous Group	11
2.3	Contact Friction	12
2.4	Carbon Fibre Rods	13
2.5	6 mm Rod vs Carbon Fibre Rods	14
2.6	Air Bearing	15
2.7	First Generation Prototype	16
2.8	Second Generation Prototype	20
2.9	Final Design Overview	22
2.10	Front Lighting	23
2.11	Back lighting	24
3.1	MATLAB Algorithm for Finding Particles	28
3.2	MATLAB Particle Tracking Software Activity Diagram	31
3.3	Shock Wave Experimental Footage	33
3.4	Shock Wave Particle Trajectories	33

List of Figures

3.5	Acoustic Wave Experimental Footage	34
3.6	Acoustic Wave Particle Trajectories	35
3.7	Pre-compression Wave Experimental Footage	36
3.8	Pre-compression Wave Particle Trajectories	36
4.1	Magnets on Rod for Simulator	40
4.2	9300 FPS Dynamic Loading Footage Snapshot	43
4.3	Dynamic Loading Magnet Trajectories	44
4.4	Static Loading Tests	45
4.5	Final Magnetic Force Potential	48
4.6	Shock wave: Reality vs Simulation	49
4.7	Acoustic wave: Reality vs Simulation	49
4.8	Expansion wave: Reality vs Simulation	50
4.9	Pulse/Wave Speed v.s. Magnet Separation for Given Initial Velocities	53

List of Tables

2.1	Specifications of first and second-generation air bearing system	21
4.1	Dynamic loading test cases	43
A.1	Set 1	61
A.2	Set 2	62
A.3	Set 3	62

Chapter 1

Introduction

1.1 Different Regimes of Particular Interaction

On the atomic or molecular scale, all particles exert both attractive and repulsive forces on each other. Gas particles are widely separated from one another, and have weaker intermolecular bonds than liquids and solids. The intermolecular forces result from electrostatic interactions between the particles. In particular, like-charged gas particles repel, while oppositely charged regions of different gas particles attract one another. Gaseous compounds with polar covalent bonds - such as hydrogen, H_2 , contain permanent charge imbalances and experience strong intermolecular forces. Electrostatic attraction and repulsion between electrically-charged particles is the strongest of all intermolecular forces. These are often called coulombic forces and cause opposite charges to attract and like charges to repel.

Somewhat similar to Sir Isaac Newton's inverse-square law of universal gravitation, Coulomb's law, or Coulomb's inverse-square law Coulomb (1785) describes the electrostatic interaction between charged particles as "The magnitude of the electrostatic force of interaction between two point charges is directly proportional to the scalar multiplication of the magnitudes of

Introduction

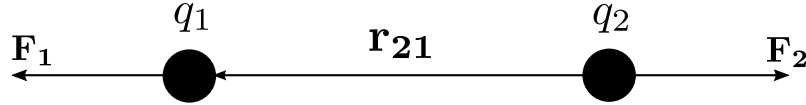


Fig. 1.1 Coulomb's force of repulsion for two like charges

charges and inversely proportional to the square of the distance between them.” This law applies to both repulsive and attractive electrostatic forces between the particles. This relation is given by

$$F = \frac{k_e q_1 q_2}{r^2}, \quad (1.1)$$

where k_e is Coulomb’s constant, q_1 and q_2 are magnitudes of the electrostatic charges, and r is the separation between the particles.

Another interesting regime is the particular interaction in granular media, where particles are in contact with one another. Granular materials provide an example of media where linear, and even weakly nonlinear descriptions, fail. Their interaction law is highly nonlinear and governed by what is known as the Hertz law: force developing under the compression of two elastic granules has no linear part, and the material has no tensile strength (see Figure 1.2).

The interaction law dictates a nonlinear potential when the granules are in contact, and zero interaction force under tension if there is no contact. The Hertz Law for two spherical granules is given by Nesterenko (2001):

$$F = \frac{2E}{3(1-v^2)} \left(\frac{R_1 R_2}{R_1 + R_2} \right)^{\frac{1}{2}} ((R_1 + R_2) - (x_2 - x_1))^{\frac{3}{2}}, \quad (1.2)$$

where F is the compression force between granules, E is Young’s modulus of the material, R_1 and R_2 are the granule’s radii, v is the Poisson coefficient, and x_1 and x_2 are the coordinates

1.1 Different Regimes of Particular Interaction

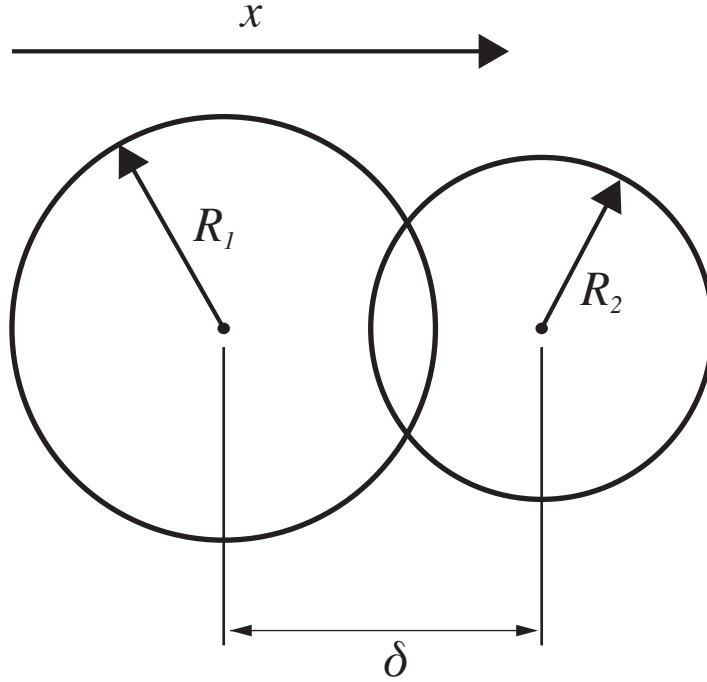


Fig. 1.2 Hertz law describes the compression force between two granules in contact

of the spherical granules centres. The dependence of F in the form of $\delta^{\frac{3}{2}}$, where δ is the approach of particle centres, is valid for spherical granular contact (Landau and Lifshitz, 1959).

Much more generally, the Hertz law is given by Landau and Lifshitz (1959)

$$V(\delta_{k,k+1}) = \frac{a}{n} |\delta|_{k,k+1}^n, \quad \delta \leq 0, \quad (1.3)$$

$$V(\delta_{k,k+1}) = 0, \quad \delta > 0.$$

Here

$$\delta_{k,k+1} \equiv y_k - y_{k+1}, \quad (1.4)$$

where a is a constant that depends on the Young's modulus and Poisson's ratio, and y_k is the displacement of granule k from its equilibrium position. The exponent n depends on geometry.

Introduction

Lastly, when looking at material as a macroscopic scale, discrete particles become continuous. In this regime, the interaction law between the infinitesimal quantities can be well-approximated using a linear relationship:

$$F = kx, \quad (1.5)$$

where k is the stiffness or spring constant of the material, and x is the displacement from equilibrium. Equation 1.5 is known as Hooke's law.

1.1.1 Pulse Velocity for Beads-on-a-Wire

At an atomic scale, the distance between two gas particles is generally very large comparing to their interaction potential. That is, two particles' influence on one another is very small until they get relatively close, at which point the repulsive force becomes very large. This causes what appears to be a perfect elastic collision between them, somewhat similar to billiard balls, or beads on a wire. In this regime, a disturbance, or an impulse, propagate through the system at a velocity v_{pulse} that is the same as the translational velocity of the particle responsible for the propagation:

$$v_{pulse} = v_{particle}. \quad (1.6)$$

1.1.2 Pulse Velocity in Nonlinear Chains

Pulse velocity in a frictionless, nonlinear, granular chain is an area of active research (Nesterenko, 1983, 1995; Rosas and Lindenberg, 2004). In short, continuum approximations can be made to obtain quantitatively accurate results for the pulse velocity in discrete granular chains with

1.1 Different Regimes of Particular Interaction

relatively soft interactions, such is the case for spherical granules. The pulse velocity is given by Nesterenko (1995); Rosas and Lindenberg (2004)

$$v_{pulse,c}(n) = \sqrt{\frac{2}{n}} \left[\frac{n^2(n-2)}{2(n+2)\sqrt{\frac{n(n-1)}{6}} I\left(\frac{4}{n-2}\right)} \right]^{\frac{n-2}{2n}}, \quad (1.7)$$

where n is the Hertz law exponent. It is important to note that for hard materials, where $n \gtrsim 3$, Equation 1.7 is no longer applicable. The pulse becomes too narrow for continuum theories, and the binary collision model becomes quantitatively accurate, and is given by Rosas and Lindenberg (2004); Wu (2002)

$$v_{pulse,b}(n) = \frac{1}{\pi^{1/2}} \left(\frac{4}{n} \right)^{1/n} \frac{\Gamma(\frac{1}{2} + \frac{1}{n})}{\Gamma(1 + \frac{1}{n})}. \quad (1.8)$$

With Equations 1.7 and 1.8, it is possible to obtain the pulse velocity in discrete granular chains for the entire range of potentials.

1.1.3 Pulse Velocity in a Continuous Spring

Pulse velocity in a continuous spring, such as a slinky, is well defined since the material is continuous. Using derivation outlined in Huggins (2008), it is relatively painless to obtain

$$v_{pulse} = \sqrt{\frac{K_{total}L}{\mu}}, \quad (1.9)$$

Introduction

where K_{total} is the total spring constant, L is the length of the spring, and μ is the density. Using the same logic, it is also possible to obtain the speed of sound in air because it could be modelled as a spring with K approximately given by $K = \gamma \cdot p$:

$$v_{sound} = \sqrt{\gamma \cdot \frac{p}{\rho}} \quad (1.10)$$

where γ is the ratio of specific heats of air at a constant-pressure to air at a constant-volume (C_p/C_v), p is the pressure, and ρ is the density.

1.2 Concept

Like electrostatic forces between particles, the interaction of magnetic poles is governed by electromagnetic fundamental force. The interaction force is given by

$$F = \frac{\mu q_{m1} q_{m2}}{4\pi r^2} \quad (1.11)$$

where q_{m1} and q_{m2} are the magnitudes of magnetic poles, μ is the permeability of the medium, and r is the separation between the poles.

Comparing Coulomb's Law (Equation 1.1) and the force between two magnetic poles (Equation 1.11) it is clear that both are proportional to the square of the distance between the poles or particles. In fact, this is the expected result as both manifestations of the same fundamental interaction.

Thus, if a physical system is constructed that could allow free magnetic interaction, the system could be used to mimic intermolecular interaction. At the same time, it may also be used to observe granular-like interaction if the separations between the poles are such that

nonlinearity in the potential is prominent. Lastly, if the poles are spaced closely apart, the system might be described as continuous.

Therefore, this study aims to create a physical system with above properties using magnets that freely interact. This can be achieved by reducing system complexity to one-dimensional, and employing unique systems such as air bearings to reduce the dissipation. Experiments can be conducted to gain understanding of wave propagation in different regimes with one physical system.

1.3 Outline

The rest of this report will first introduce the design of the experimental apparatus, where the air bearing system would be discussed. Then, the particle tracking methods and the resulting data would be shown. After that, the numerical model of the system would be presented, as well as the continuum modelling. Lastly, conclusion and future work are described at the end of the report.

Chapter 2

Experimental Apparatus

2.1 Definition

It is clear now the system's purpose is to simulate nonlinear intermolecular interaction between particles using magnets as a mechanical analogue. Hence, there are some constraints and parameters that must be met for the simulation to be valid. Every design decision is made to increase the validity, and the physical resemblance to gas particles. However, not all aspects of the target system can be replicated, but the resemblance is brought about in the best of ability.

Some of the important parameters and constraints are outlined below.

Simulating two-dimensional or three-dimensional gas particle interaction would theoretically require a surface or a volume, respectively, of free-interacting magnets. Building such systems would be tremendously difficult, and a one-dimensional system would offer significant advantages in terms of simplicity of construction and modelling. Hence, the device would be required to restrict the particles to travel in one degree of freedom.

In a mechanical system, external forces such as gravity and friction are usually present. Theoretically, particles in a one-dimensional gas would interact with each other purely

Experimental Apparatus

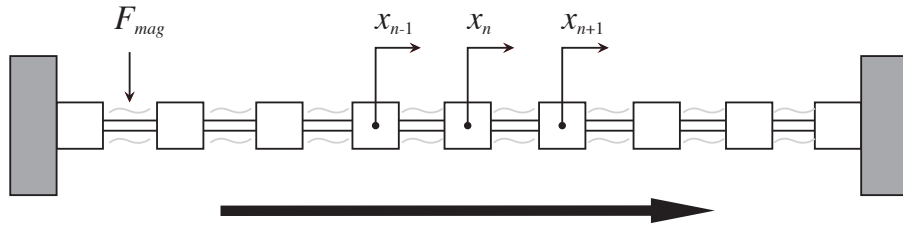


Fig. 2.1 Magnets as a mechanical analogue for one-dimensional gas particles. F_{mag} is the repulsive magnetic force acting between two neighbouring magnets. The particles' coordinates are indicated with by x_n . The two magnets on the ends of the chain are fixed to the boundary. The arrow at the bottom shows the direction of positive x .

with intermolecular forces (see Chapter 1) without the influence of gravity (whose effect is very small comparing to the electrostatic forces) and friction. Thus, the device is required to be built to eliminate as much gravity and friction as possible.

In order to eliminate the effect of gravity, the magnets would essentially have to travel horizontally. This eliminates the differential in equilibrium spacing between the magnets, which is analogous to density gradient in an ideal gas-like media.

The system should allow the experimental data to be captured easily, through the use of high-speed cameras or other sensors.

Since no real magnets would act as ideal magnetic poles, the magnets used in the system should have as little irregularities as possible. That is, the best magnet would be one that interact with other magnets with strictly inverse-square force potential.

A previous group has already constructed the frame and other elements that laid the foundation for this project. However, the problems of gravity, friction, and data capture were not resolved. Their report is found with Caplan et al. (2012).

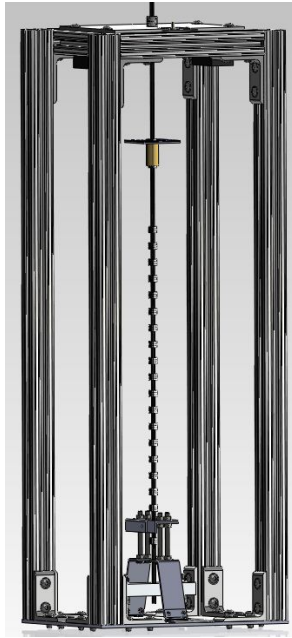


Fig. 2.2 Final design of the mechanical engineering project group

2.2 Previous Design

The mechanical engineering project group's final design can be seen in Figure 2.2. The device is upright, therefore the effect of gravity is prominent in the system. At the same time, friction effects were still present in the system, as evidenced by quick dissipation of particles' energy in the captured footage. Lastly, the footages were not suitable for analysis as they were often too dark, or the reflection of the light on the magnets distorted

2.3 Challenges and Focus

The main challenge, and the main focus, of designing the new system was to eliminate the friction caused by the contact between the magnets and the rod in the middle. In the meantime, a method to better capture and analyse experimental data was needed. Hence, the important aspects of the final design is broken down as:

Experimental Apparatus

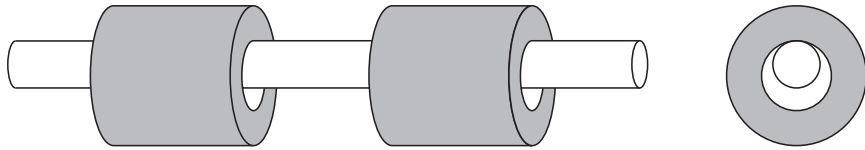


Fig. 2.3 Horizontal orientation increases contact between magnets and rod. Figure is not to scale.

- Magnets and rod
- Air bearing system
- Lighting and camera

2.4 Magnets and Rod

One of the things that the previous group missed was to eliminate the effect of gravity. Their device was upright, and the magnets travelled vertically. They did this to minimize contact time between the magnets and the rod. However, like discussed before, this also caused what is analogous to density gradients in the “gas.” Of course, this meant that their results were difficult to analyse because density gradients do not naturally occur in a gas. All density gradients would disperse, causing the resulting medium uniform in density. For this iteration of the design, the first thing to do was to lay the device on its side. Of course, this caused the problem of the magnet directly contacting (See Figure 2.3) the rod, which dramatically increased the friction.

It became unclear how the new-found friction could be eliminated. The first thing to come into consideration was replacing the rod the magnets rode on. In the previous design, due to the manufacturing tolerances of the magnets and rods - undersized inner diameter (ID) of the magnets and oversized outer diameter (OD) of the rods - a bundle of four 3/32” OD carbon



Fig. 2.4 Previous design of using four carbon fibre rods.

fibre rods were used. While this was an acceptable solution for when the device was upright - the rods provided relatively smooth motion - the increased contact and the non-circular cross section meant that they were not able to deliver functional, friction-free motion for the magnets.

The magnets have already been chosen to be 1/2" by 1/2" with 1/4" ID. These dimensions are ideal for simulating magnetic poles due to the uniformity of the length and width (the force potential will be discussed in Section 4.1.1). However, as the inner diameter of these magnets is generally manufactured to be undersized, a replacement rod could not be 1/4" in diameter. Various methods of altering the diameters were considered: drilling out the magnets, sanding the rods down, and lathing the rod to a smaller diameter. However, these plans were quickly abandoned as challenges arose: the magnets are made of neodymium alloy, which is very brittle, and cannot withstand drilling without cracking; sanding and lathing the rod were considered too labour intensive and could introduce non-uniformities along the length of the rod, which could cause the magnets to *jump* as they slide. This meant that another idea was needed.

2.4.1 The 6 mm Acrylic Rod

Because the carbon fibre rods do not offer satisfactory performance when the device is horizontal, an alternative centrepiece was needed. Since $1/4" = 6.35 \text{ mm}$, using a 6 mm instead of 1/4"

Experimental Apparatus

rods began to look like a much better solution (see Figure 2.5). Even given dimensioning tolerances, the $0.35/2 = 0.175$ mm gap is large enough that manufacturing discrepancies are not a concern.

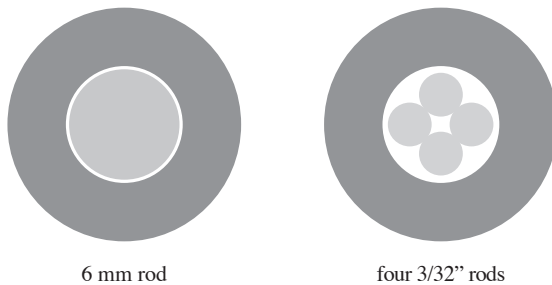


Fig. 2.5 Cross-sectional view of new rod versus four carbon fibre rods. The 6 mm rod would allow more uniform contact between the magnets and the rod.

The motion of magnets, and their magnetic fields, would induce eddy currents in conductive objects nearby. This rules out the possibility of using metallic rods as the eddy current would create an opposing magnetic field to the magnets, which creates undesirable external forces.

Unfortunately, most manufacturers in North America do not offer non-conductive rods of made in SI standards. Some suppliers offered 6 mm metallic rods, but all plastic rods were only manufactured to common fractions of the inch. It was possible to have some suppliers custom-make the rods, but that was determined to be too cost-ineffective. From there, the only obvious way to obtain these rods was to look to Europe. Fortunately, many plastic suppliers in Europe carried 6 mm plastic rods, but only ones made with acrylic.

The search for better prices led to a new discovery - 6 mm OD/5 mm ID acrylic tubes were also available. This then led to next phase of the project - it may be possible further reduce friction by creating an air bearing system with the tube as the centrepiece.

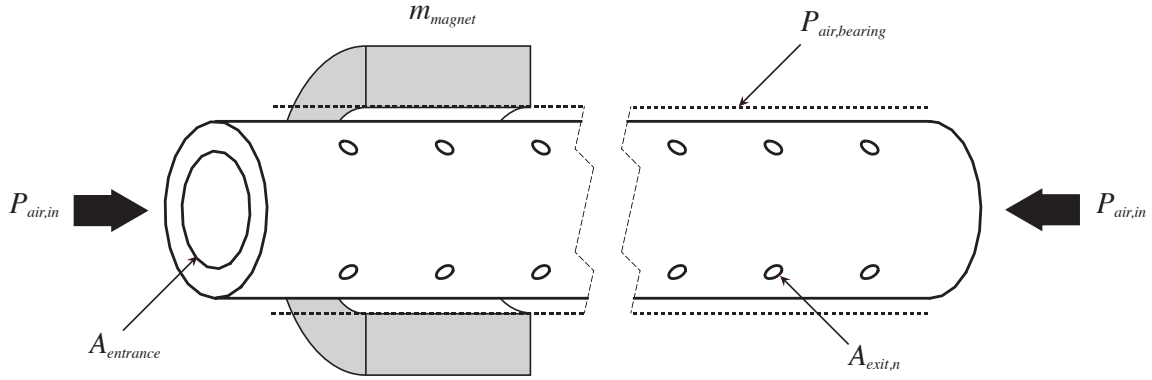


Fig. 2.6 Diagram for how the air bearing system could be implemented. $A_{entrance}$ is the cross-sectional area of the two entrances of the tube, $P_{air,in}$ is the pressure for the input air on both ends, and $P_{air,bearing}$ is the pressure for the thin air film created by air exiting the n laser drilled holes of area $A_{exit,n}$.

2.5 Air Bearing System

Air bearings use a thin film of pressurized air to provide low friction interface between surfaces. The two surfaces do not touch and are essentially contact-free. The thin film is air that flows from the bearing to the surface. Although the air constantly escape from the nozzles, the pressure between the contact surfaces is enough to *suspend* the load. Air bearings are extensively used in industry to avoid problems such as friction, wear, and lubricant handling.

As air bearings are mainly used in precision machinery tools and fast running machines, commercially available varieties are not viable for the subject application. Also, most off-the-shelf air bearings are made of metal (usually steel) which render them unsuitable. Thus, a custom-made system was in order.

One of the type of air bearing is the laser-drilled micro nozzle bearing. It makes use of computerized manufacturing technology to create lots of micro nozzles to achieve effectively uniform pressure distribution within the air gap. At the same time, labour costs are greatly reduced and repeatability is increased. It made sense to use the same technique to create the

Experimental Apparatus

desired custom air bearing system for the subject study. The acrylic tube would be evenly laser drilled to create a perforated, almost porous, surface profile. Research on local laser drill service providers showed that this is a real possibility as acrylic is perfect for laser operations¹. The service also reported that hole diameter of 0.2 mm is possible.

Immediately, work began to make the air bearing a reality (see Figure 2.6 for the concept). Some² 6 mm OD/5 mm ID acrylic tubes were sourced from the UK (at a hefty shipping cost). The laser drilling supplier was contacted to perform the perforation of the tubes. For the preliminary feasibility study, it was decided that the tube should be drilled with rounds of 8 holes spaced about 6.35 mm from the next. The tube was to be 1 meter long.

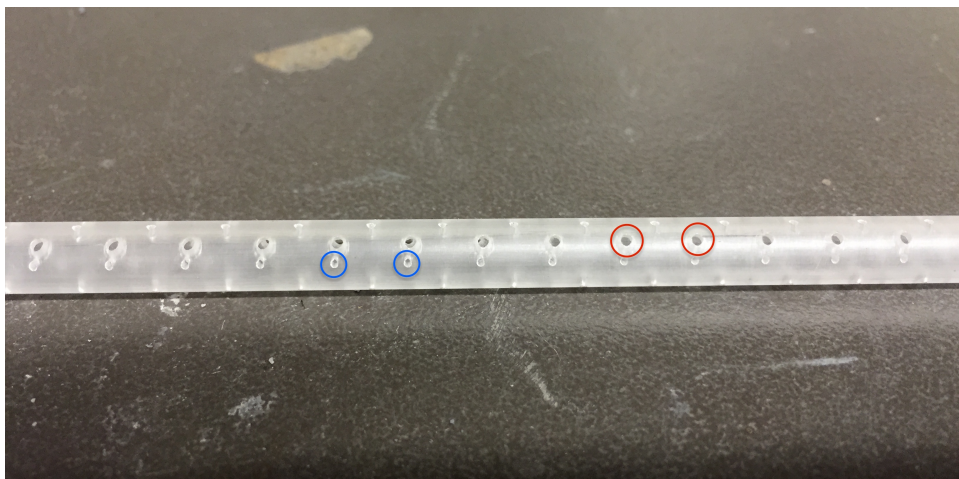


Fig. 2.7 First generation air bearing tube. Note the much smaller entry holes (indicated by blue circles) comparing to the exit holes (red circles). The entry holes are 0.2 mm in diameter and the exit holes are 1.0 mm in diameter. The exit holes are 25 times the size of the entry holes.

After some negotiating with the supplier about manufacturing concerns - precision, tooling, and jigs needed - the first-generation prototype was completed. However, in order to save time, the tube was drilled all the way through so that one puncture would create two holes - one at the entrance and one at the exit. This strategy was discussed prior to the manufacturing and agreed

¹unlike other plastics such as PVC, which give off toxic fumes under high heat

²10 tubes total were purchased

on. Unfortunately, as seen in Figure 2.7, the exit holes are much (roughly 24 times larger by area) larger than the entrance holes. This result was not expected, but it was not immediately clear if it would be a problem, so the rest of the setup was completed first. Air regulators, hoses, and clamps were purchased so that air could be pumped into the tube from shop air supply line.

The first test was conducted. Air was routed from the supply line to the regulator and then routed to *one end* of the tube. Results were disappointing: the exiting air was much stronger at the entrance side and tapered off promptly along the length of the tube. No air was exiting the perforation after the middle point of the tube.

However, one thing was promising: near the entrance of the air supply, the first one or two magnets began to suspend. It was actually possible to put a spin on the magnet and it would continue to do so - for a significant amount of time due to the reduced dissipation. This was an uplifting result.

A question was raised: what could be done to eliminate the tapering air flow profile? That is, is it possible to deliver enough air into the tube so that every exit hole is saturated with air flow? It was clear that the large exit holes would need be eliminated, but it was not clear if that would promise uniform pressure distribution along the entire air bearing core.

2.5.1 Uniform Flow

The effect of maximum air flow is known as *choking*. Essentially, when air at a given pressure and temperature passes through a restriction, there is a limiting condition where the mass flow rate will not increase with a further decrease in the downstream pressure. At that point, the flow becomes a choked flow. However, the mass flow can be increased by increasing the upstream pressure. This concept is critical for the air bearing system in subject.

Consider small exit holes along the air bearing core. Relatively, a large amount of air \dot{M} travels down the inside of the tube and attempt to exit into the atmosphere (because the

Experimental Apparatus

downstream pressure here - atmospheric pressure - is much lower than the upstream pressure) through each of the small restrictions created by laser drilling. Since the total mass flow rate is a function of driving pressure, theoretically if the upstream pressure can be increased indefinitely, the air flow will incrementally become choked at each exit. That is, with some large pressure P inside the tube, *all* exits should become choked with the same mass flow rate of \dot{m} given by

$$\dot{M} = N\dot{m}, \quad (2.1)$$

where N is the number of exit holes. Because all the exit holes are the same size, at this point all exits would have the same amount of air flow passing through, an uniform pressure distribution along the entire length of the tube can be achieved.

However, it is *not possible* to increase the air pressure inside the tube indefinitely. If the inside pressure increases beyond the yielding stress of acrylic³, the tube would break. Also, the shop air supply is limited to 100 psi - a maximum for pressure at any location of the system.

A more concerning issue is that if the flow chokes at the entrance *before* completely saturating every exit, uniform air distribution can never be achieved. Increasing the air supply pressure would not improve the situation, because the \dot{m} required to choke the exits would also increase proportionally. Therefore, the only way to ensure all exits to be choked is to check if enough air can be delivered into the tube such that $\dot{M} \geq N\dot{m}$. Since the number of holes N is fixed, and \dot{M} and \dot{m} are both functions of the same driving supply pressure P_0 , the relationship between the entrance restriction area $A_{entrance}$ and the individual hole size $A_{exit,n}$ can be defined as

$$\sum_{n=1}^N A_{exit,n} < A_{entrance}, \quad (2.2)$$

³which becomes much smaller due to the stress concentration near the laser drilled holes

2.5 Air Bearing System

which allows the solution for N , the maximum number of holes allowed. Since N should be maximized for better perforation and air bearing performance, it is clear the the individual exit hole size $A_{exit,n}$ should be minimized. Hence, large exit holes seen in Figure 2.7 could not be accepted.

In the case of this experiment, the individual hole sizes are defined by the manufacturing constraint, which dictates that the diameter of the hole is 0.2 mm. At the same time, the entrance cross sections are also defined by the inner diameter of the air bearing tube, which is 5 mm. Simple arithmetics applied to Equation 2.2 can deduce the number of holes N is

$$\sum_{n=1}^N A_{exit,n} < A_{entrance} \quad (2.3)$$

$$\sum_{n=1}^N \frac{\pi D_{exit,n}^2}{4} < \frac{\pi D_{entrance}^2}{4} \quad (2.4)$$

$$0.2^2 N < 5^2 \quad (2.5)$$

$$N < 625, \quad (2.6)$$

which is smaller than the number of holes drilled in the first generation prototype (Figure 2.7) - 1256 holes⁴. It was concluded that if air was supplied to *both ends* of the tube, doubling the entrance cross-sectional area, and then omitting the ends from the drilling process, the number of holes can be brought to an appropriate number: $1250 = 2N$ holes⁵. It was hypothesized that this should create the uniform pressure distribution desired. Since solving the system analytically or numerically simulating the system using computational fluid dynamics appeared

⁴157 rounds of 8 holes = 1256 holes.

⁵The combination of the ID being 5 mm, holes being 0.2 mm, and 1 mm length was almost ideal, which was a pleasant surprise.

Experimental Apparatus

to be time-consuming as well as out of the scope for the project, the better option was to simply prepare the second-generation iteration and see if it would work.

2.5.2 Second-Generation and Final Design Overview

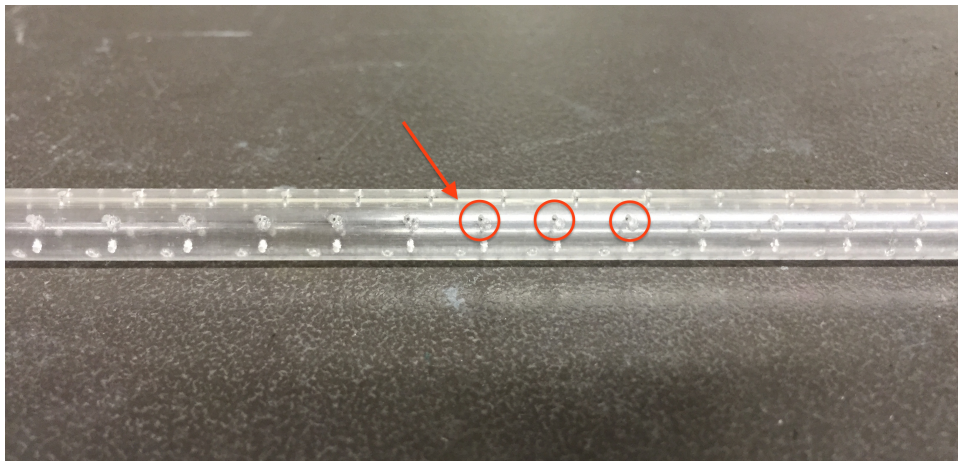


Fig. 2.8 Second generation air bearing tube. The red arrow indicates typical laser drilled holes. Precautions were taken to ensure that only entry holes registered on the tube. The holes are 0.2 mm in diameter.

For the second-generation device, the design specifications remained roughly the same as those intended for the first-generation iteration. Table 2.1 shows the specifications in detail. It was theorized that the first-generation device was almost suitable for the experiment had the large laser exit holes not existed. With that, the supplier was again contacted. A manufacturing procedure was introduced to eliminate the exit holes: a simple 1 m long wooden rod inserted into the middle of the tube prevents the laser from puncturing all the way through.

Within days, the renewed tube was received. Figure 2.8 shows the updated air bearing tube. As expected, all holes on the tube were 0.2 mm in diameter. Therefore, the prototype should be able to deliver uniform flow to the system.

2.5 Air Bearing System

Table 2.1 Specifications of first and second-generation air bearing system

Property	Generation I		Generation II	
	Design	Actual	Design	Actual
Length	1 m	1 m	1 m	1 m
Number of Holes	1256	1256	1250	1250
Hole Diameter	0.2 mm	0.2 - 1 mm	0.2 mm	0.2 mm
Holes Per Round	8	8	8	8
Round Separation	6.35 mm	6.35 mm	6.35 mm	6.35 mm
Air Input	100 psi single	80 psi single	5 - 60 psi double	5 - 60 psi double

At the same time, a new system of air input was developed. The system consists of an air regulator⁶, a Y-connector to split the air supply into two, and hose clamps to secure the hoses onto the ends of the air bearing tube. The overview of the system can be seen in Figure 2.9.

Some tests were conducted to evaluate the performance of the new device. The air input system was mounted on both ends, the hose clamps secured, and the air supply turned on. The air regulator pressure was increased slowly - and the magnets began to suspend. The air distribution appeared to be uniform along the length of the tube when felt by hand. Once the air regulator read 60 psi, all the magnets seemed to be completely suspended. It was possible to spin individual magnets for a long period of time. In other words: the second-generation device was successful in meeting the requirements of minimization dissipation.

From there, it was determined that the air bearing system is suitable for experiments. The results can be found in Chapter 3.

⁶The maximum air flow rate was determined to be sufficient.

Experimental Apparatus

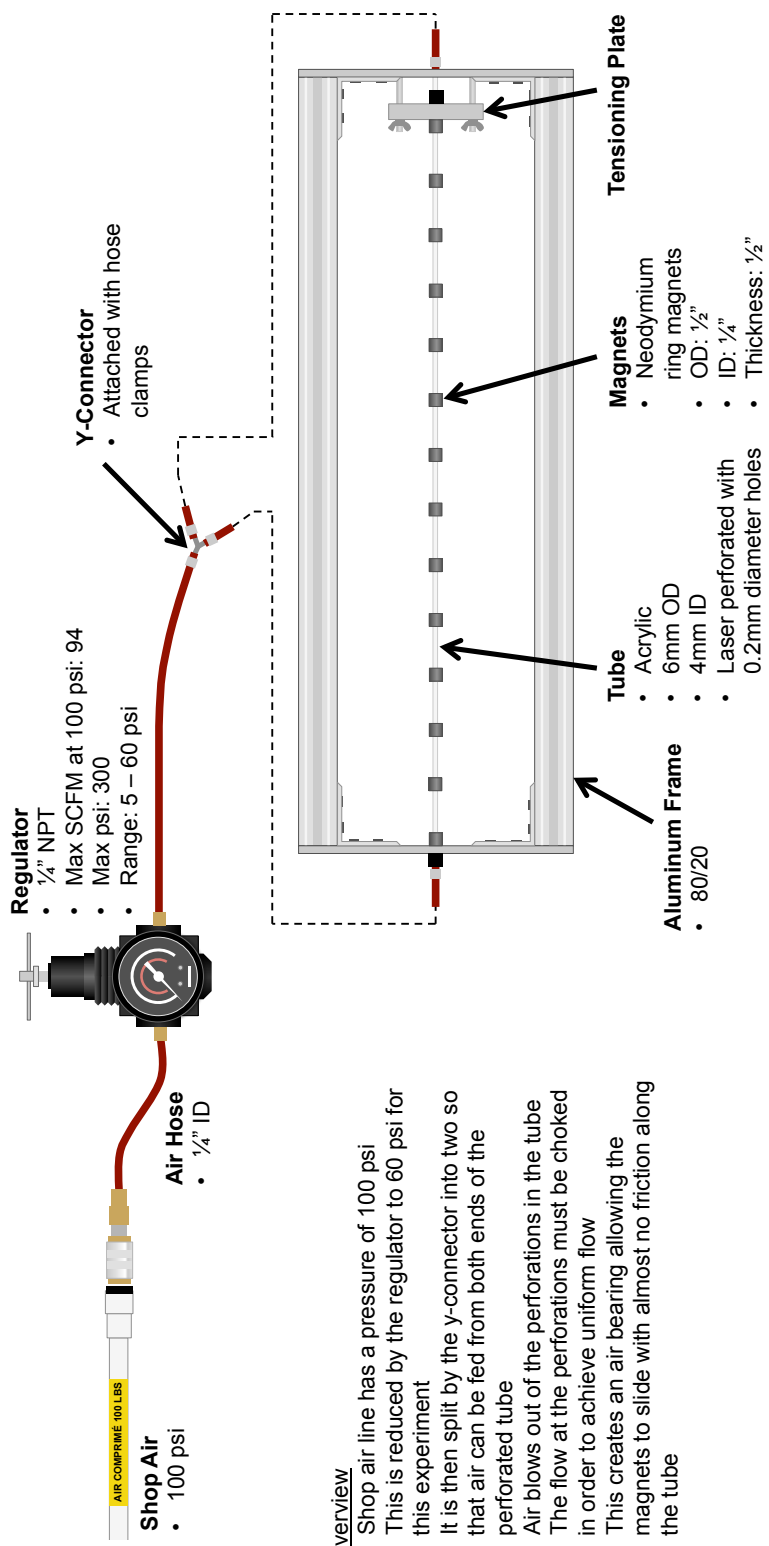


Fig. 2.9 The overview of the final design and specifications. Diagram courtesy of Douglas Prisnie.

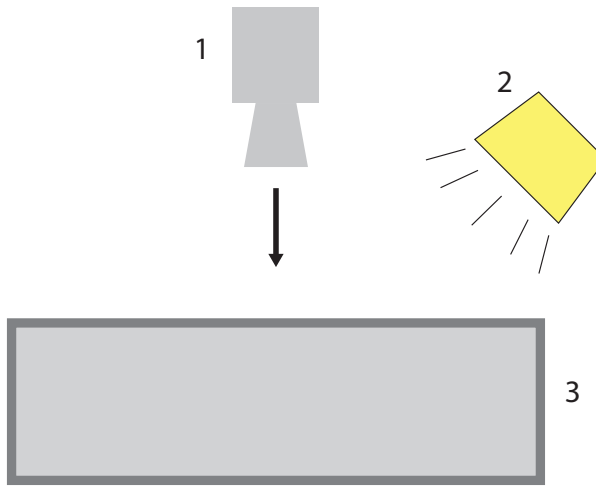


Fig. 2.10 Overhead view of the experimental setup with front lighting. Item (1) is the high-speed camera, (2) is the 500 W light, and (3) is the experimental device.

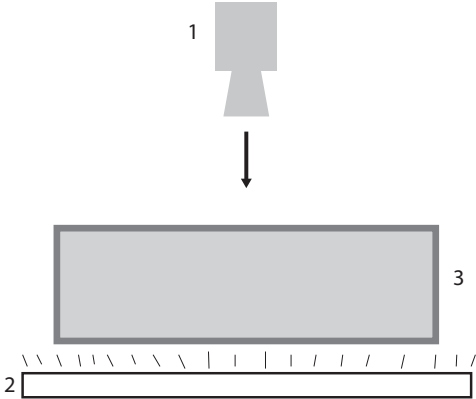
2.6 Lighting and Camera

Along with the experimental apparatus, a system to capture and analyse data is also needed. It would be important to have optimal lighting and camera to convert real world motion into digital photography & data.

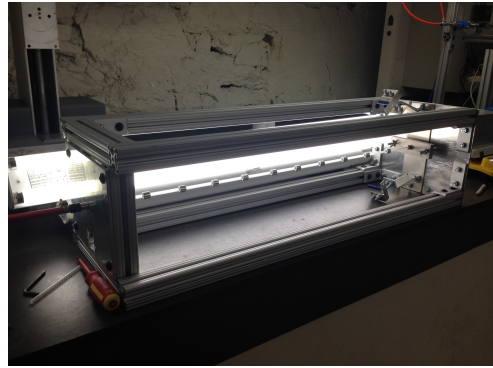
To that end, multiple systems were considered. The first one to be considered was the front-lighting system. It was considered because it was the most obvious solution. Lighting from the front was easy to do and there were already some high-power industrial lights available. The lights were 500 W, and extremely bright. At the time, it seemed like no other options were even considerable. See Figure 2.10 for the set up.

Different cameras were also considered. One of them was the Photron SA5 camera, which could capture footages up to 10,000 FPS with 1 mega pixel resolution. It was a popular camera but used whenever possible. The other camera was an ordinary Casio camera with the ability to

Experimental Apparatus



(a) Back lighting set up. Item (1) is the high-speed camera, (2) is the 500 W light, and (3) is the experimental device.



(b) View of the experimental system with back lighting turned on.

Fig. 2.11 Back lighting

capture 600 FPS footages. This camera was used when the SA5 was not available. However, as seen in Chapter 3, the camera was able to produce acceptable results.

The cameras were mounted on tripods to optimize stabilization.

However, it was not the optimal solution. The problem with front lighting was that the reflective surfaces of the magnets presented challenges in footage analysis. As discussed in Section 3.1, the particle finding algorithm attempts to obtain the centres of the bright spots. Since the light source is fixed and the magnets move, the bright spots shift over time, causing inaccuracies in the the positioning of the particles. Another issue was the it was very challenging to position the light in a way that all the magnets can be easily seen on film. This is because, again, the reflective surface of the magnets causes the camera to adjust the exposure levels in order accommodate the very bright, but this meant the the darker areas become very ill resolved. So some magnets are almost completely invisible for some frames. Of course, this meant that analysis was not possible.

2.6 Lighting and Camera

Eventually, it was realized that **back lighting** may be a better alternative to front lighting. Uniform back lighting - in this case, fluorescent - is ideal in showing the outlines of the magnets. Essentially, the shadows of the magnets are shown to the cameras. This eliminated the reflectiveness problem, which theoretically greatly improves the accuracy of the particle-finding algorithm. So, long, industrial fluorescent light fixtures were purchased and placed behind the experimental apparatus to create the desired effect. The set up can be seen in Figure 2.11.

Chapter 3

Experimental Results

To validate the model of magnets acting as particles, and to be able to see the different wave behaviours, there needs to be a way to reliably capture and analyse the data. Only from there is it possible to obtain information such as particles' positions over time, their accelerations, forces acting on them, and wave or pulse velocity in the chain. An obvious way to obtain this data is to use high-speed photography. The magnets' continuous motion can be captured and discretized into frames of images. Each on these images would contain the magnets' location for that given frame. Since the magnets' sizes can be determined with high accuracy, and the frame number can be converted into time by knowing the frame rate, it is possible to realize the magnets motion into discrete numerical data of positions over time. From there, the particle trajectories can be readily plotted, which would show the wave propagation - the desired information.

Set up concerning lighting and camera is discussed in Section 2.6. Once the footages were obtained, research began to find the best way to analyse them. At first, the footages were simply low-resolution, blurry videos. It was not immediately obvious how computers could recognize the moving particles and associate them into defined trajectories from one frame to the next. It

Experimental Results

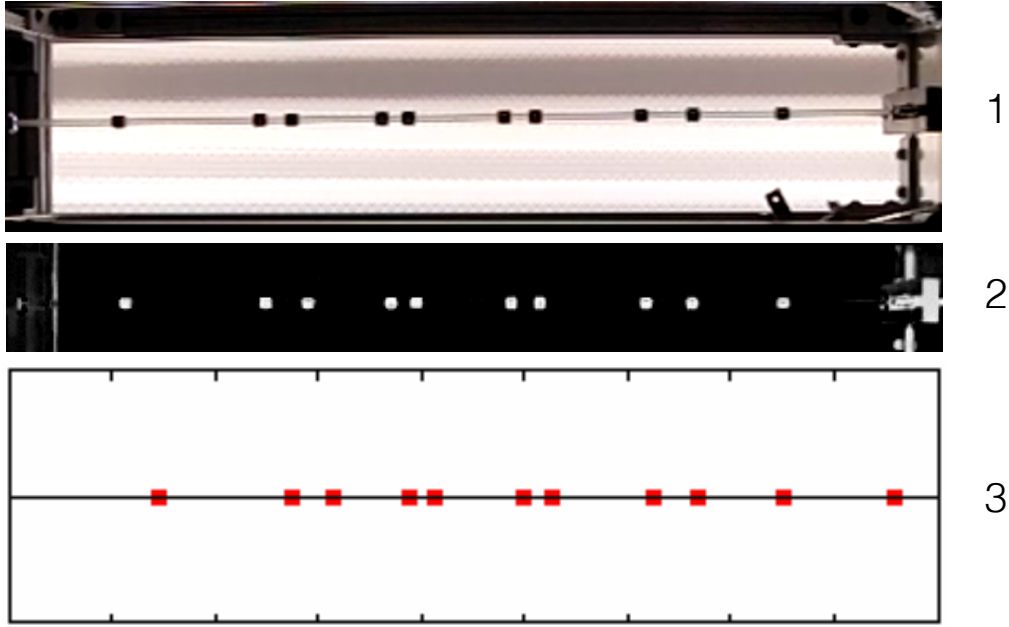


Fig. 3.1 (1) MATLAB reads in a single frame of the captured footage (note the back lighting), (2) the algorithm applies a bandpass filter to the image, isolating the bright peaks as the particles, (3) the particle finding algorithm finds the positions of the particles by looking for the locations of brightness peaks

might be obvious to a human, but how could a computer know which the the particles are related when presented with two consecutive frames?

3.1 Footage Analysis

Methods of tracking particles and their trajectories have been an area of active research in computer science. In particular, the methods presented by Crocker and Grier (1996) had since been widely cited and adopted. In fact, the authors have released a fully developed, completely free IDL implementation of the algorithm (Crocker and Grier, 2008), which has then been

3.1 Footage Analysis

translated to MATLAB by Blair and Dufresne (2008). Thanks to them, a complete MATLAB particle tracking tool has been developed for this study.

The methods developed by Crocker and Grier are largely general and applicable for 2-D motion for particles in a plane. In fact, it was mainly used to track round micro particles. For each frame of the footage, the algorithm can be used to perform:

1. Read in a single frame of footage,
2. Invert the image colour (if needed),
3. Apply image processing filters using user-specific parameters such as the bandpass which locates the bright pixels,
4. Locate the brightness peaks with given thresholds,
5. Obtain centroids of each peak with sub-pixel accuracy, and
6. Output particle positions.

Figure 3.1 shows a visualization of the process. From there, the algorithm can then link the coordinates found in each image together to form trajectories. However, a macro is needed to repeat the process for every frame of the footage. Then, it is possible to take the list of particle positions, along with the timestamp for each frame, to form the trajectories information needed¹.

Some work was needed to adapt the algorithm for the subject study. Namely:

1. The videos needed to be split into discrete images,
2. Footage specific parameters needed to be obtained,

¹With additional parameters to adjust

Experimental Results

3. Units such as frame number and pixels needed to be converted to meaningful ones such as seconds and meters,
4. The results needed to be visualized to verify the accuracy of the tracking algorithm, and
5. The tool needed to be more user-friendly and easy to learn.

It would not be very difficult to implement most of these items in MATLAB. However, since each piece of footage is unique, the specific parameters needed to produce optimal results could not be systematically obtained. This meant that it was necessary to get them through brute force, i.e. trial and error. Some of these parameters include sizes of the particles in pixels, average level of noise, number of frames the particles could be lost for, minimum number of frames for each trajectory, etc. Fortunately, it was possible to estimate some of these parameters. Therefore, to minimize the time needed to work out the parameters, the program is structured to take a family of default parameters that have proved to be reliable when the tool is used to analyse a new piece of footage. If the tool successfully runs, the default config.m file is then copied into the footage directory for future use. If the tool does not successfully run, it is easy to adjust the parameters in-file because it is human-readable. This allows for fast iterations of trial and error, which unfortunately could not be completely eliminated.

To convert the output into meaningful units, the user needs to supply some additional parameters such as frames per second (FPS) and meters per pixel. The FPS value is usually readily obtained since it is a critical value to specify when the filming is done. The meters per pixel value can be obtained by examining the footage and comparing the frame size measured in pixels to the actual physical model measured in meters. With these parameters, it is possible to obtain particle trajectories in SI units.

In order to visualize the results, an animation algorithm was developed. This algorithm works to recreate the footage, but with the tracked results. The animation proved to be crucial

3.1 Footage Analysis

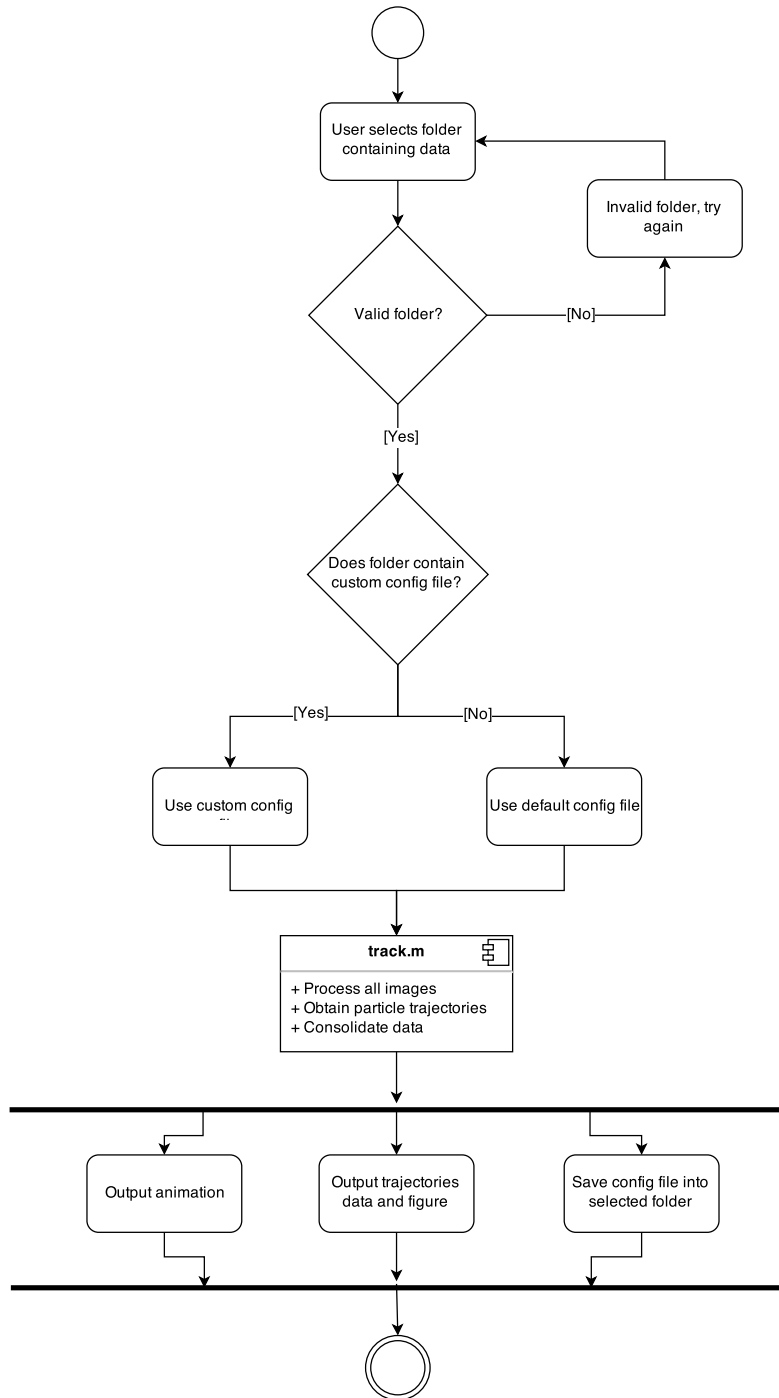


Fig. 3.2 Activity diagram of the MATLAB program used for particle tracking

Experimental Results

in analysis because the instant visual feedback can show if the tracking went successfully or not. This animation algorithm also contains code that outputs the animation in GIF format. Section 3.2 shows the results of this algorithm.

To maximize user-friendliness, the tool allows directory selection via a basic graphical user interface (GUI). Since adjusting the parameters is possible - between runs - for each piece of footage, the user does not have to worry about changing internal code when modifying the parameters. This also means that the run would successfully run every time after the first success, because the `config.m` file is stored in the same directory as the footage.

Figure 3.2 shows a simplified activity diagram for the MATLAB particle tracking tool.

3.2 Particle Trajectories

The device enabled the study of wave propagation in a one-dimensional chain. Some testing was needed to see if the reduced dissipation achieved by the air bearing was effective or not. Since - in the case of no friction at all- the magnets would interact completely freely, their trajectories can almost be intuitively predicted. Therefore, it would be worthwhile to see if the resulting trajectories match predictions.

Three different test cases were conducted: shock wave, acoustic wave, and pre-compression. These test cases were all filmed using the Casio camera at 600 FPS, and the footage was analysed by the MATLAB particle tracking tool.

3.2.1 Shock Wave

In a one-dimensional chain with identical masses, a shock wave is formed when there is a driving piston travelling at a constant velocity v . (Higgins, 2011) The shock wave would have a front travelling at $2v$. In order to simulate this phenomenon, one magnet was forcefully pushed

3.2 Particle Trajectories

at a near-constant velocity. Since all the magnets repel each other, the shock front soon began to build up.

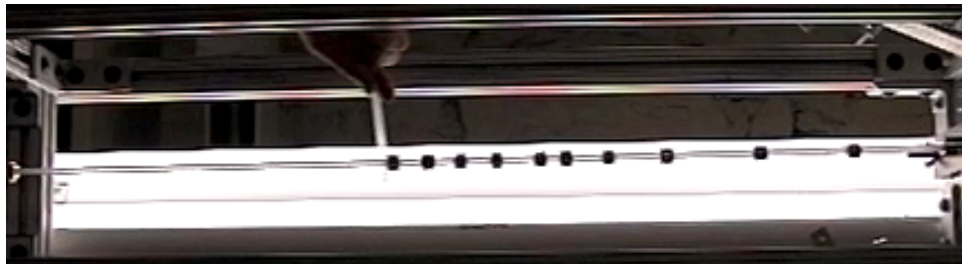


Fig. 3.3 Shock wave in discrete particles is created by a driving piston

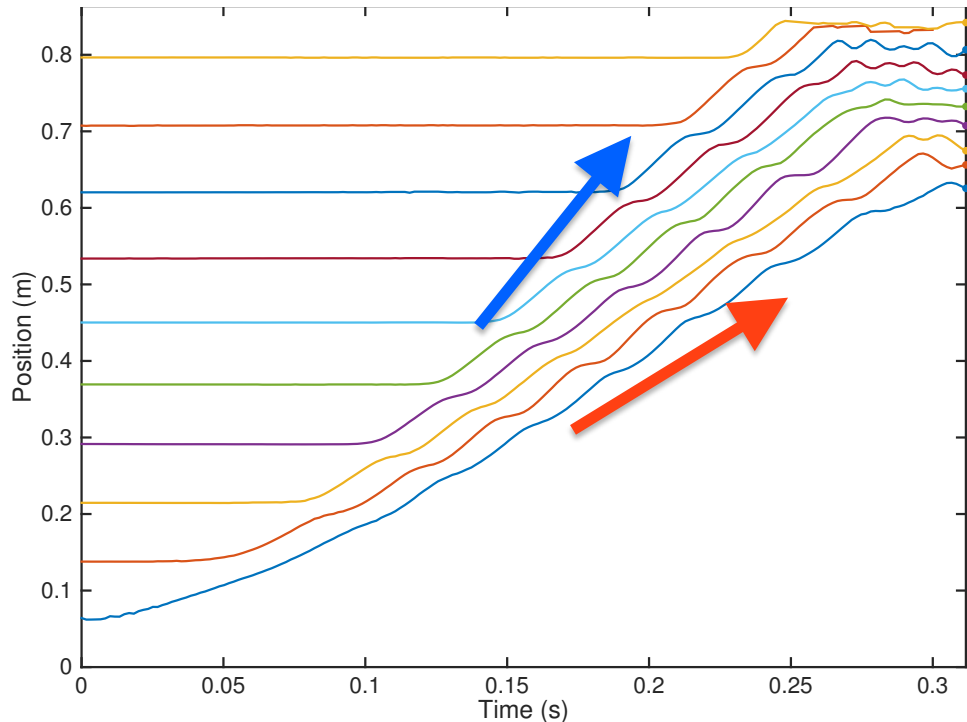


Fig. 3.4 The trajectories of the shock wave test case as tracked and recreated by MATLAB

A snapshot of the experimental footage can be seen in Figure 3.3, and the tracked trajectories can be seen in Figure 3.4. In the trajectories, it is easy to see that the initial particle remains at a near-constant velocity, while the shock front is building up quicker. The motion of the shock

Experimental Results

front can be seen as indicated by the blue arrow, and the driving piston motion is indicated by the red arrow.

It can be concluded that the system is suitable for simulating shock-like waves in a one-dimensional chain.

3.2.2 Acoustic Wave

An acoustic wave can be simulated by inputting a weak impulse into the system. The impulse triggers a perturbation that propagates through the particles. The disturbance's velocity would be the pulse velocity for the given input velocity and initial separation. This was accomplished by manually perturbing the first magnet by hand, giving it an initial velocity. The pulse can be seen travelling down the chain and back.

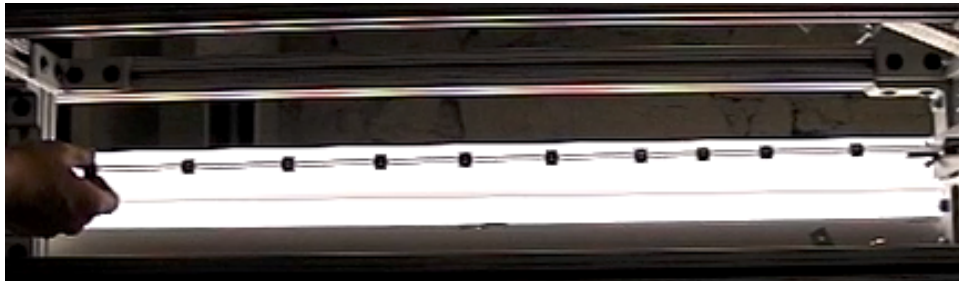


Fig. 3.5 Acoustic wave in the one-dimensional chain is created an impulse input to the system

A snapshot of the experimental footage can be seen in Figure 3.5, and the tracked trajectories can be seen in Figure 3.6. As it can be seen in the particle trajectories, the initial input velocity is lower than the pulse velocity in the media. The initial velocity of this particular experiment was determined to be 0.8 m/s, and the pulse velocity was 1.6 m/s. This result mostly aligns with the continuum modelling of the system, which will be discussed in Section 4.2.

Additionally, since friction has been greatly reduced in the system, the pulse travelled back and forth with very little decay. The trajectories plot had been edited to contain only one

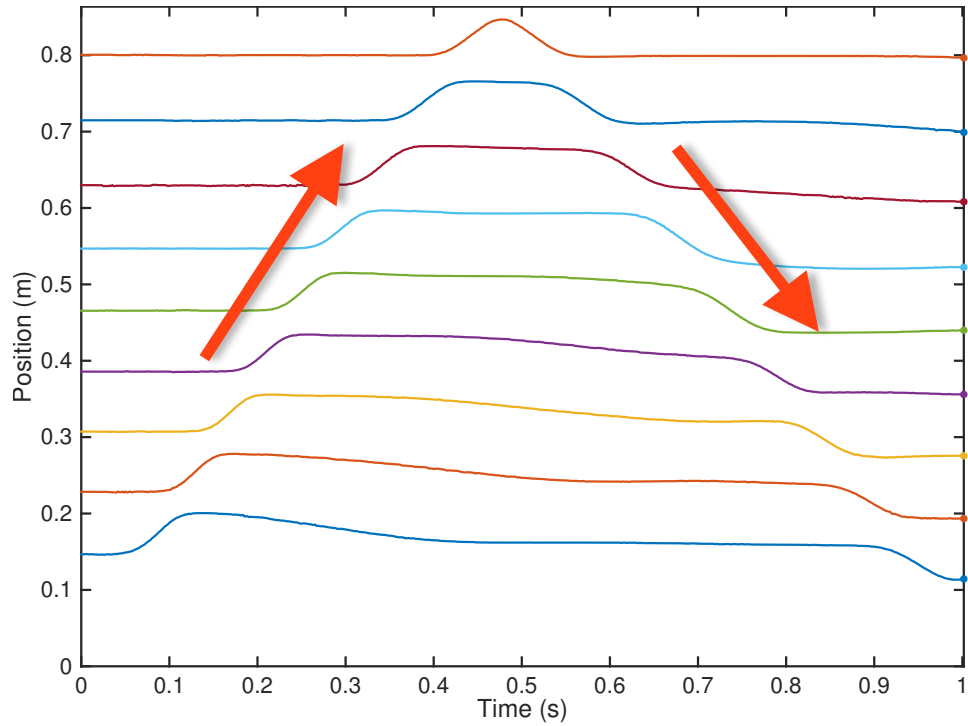


Fig. 3.6 The trajectories of the acoustic wave test case as tracked and recreated by MATLAB

rotation of the pulse for brevity. This result is what would be expected for a free-interacting one-dimensional chain.

3.2.3 Pre-compression

The pre-compression test case is used to simulate expansion waves. The magnets - particles - were held in place by the compression arms. A pin was inserted to keep the particles compressed. This created a region of high density, high potential energy particles as opposed to the low density ones outside the compression. Similarly, a shock tube has a region of high density, high energy gas behind a diaphragm. As the simulation begins, the pin is pulled and the compression arms were released, simulating the breaking of the diaphragm. The high energy particles expanded or rushed to the low density region.

Experimental Results

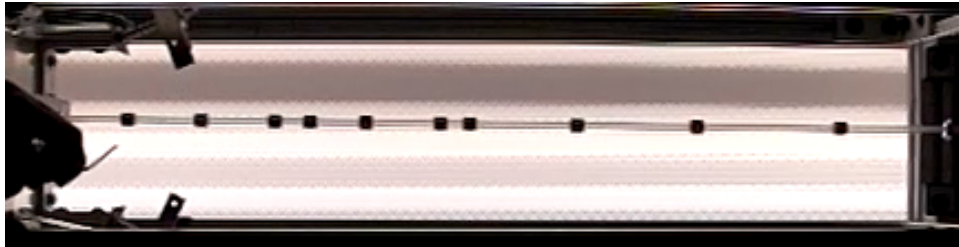


Fig. 3.7 Pre-compressing some magnets in the one-dimensional chain creates dynamics that mimic breaking a diaphragm

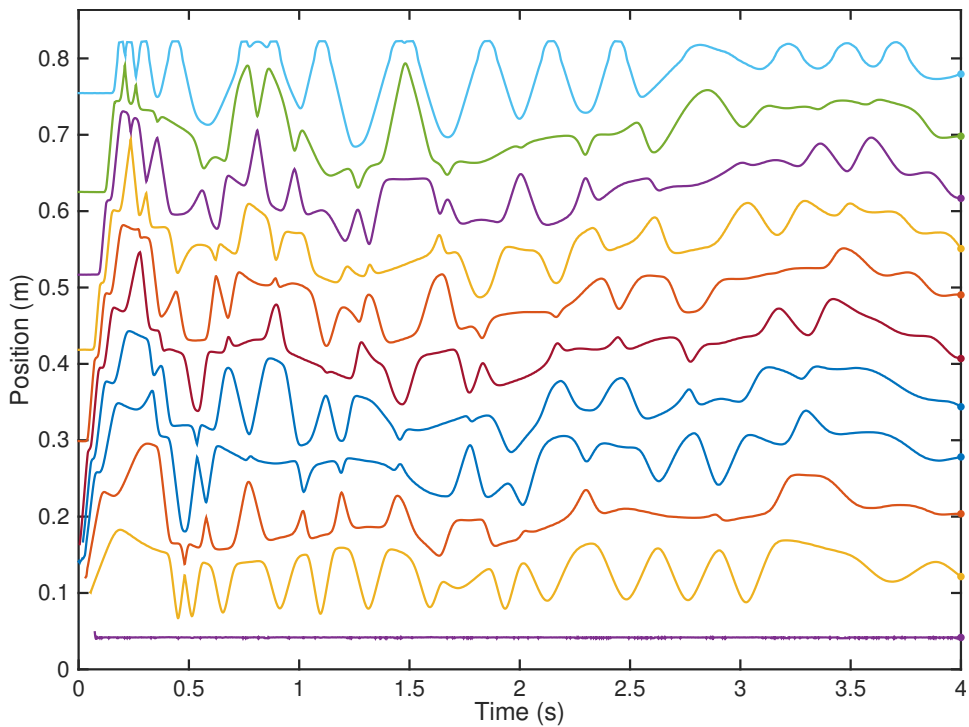


Fig. 3.8 The trajectories of the pre-compression test case as tracked and recreated by MATLAB

A snapshot of the experimental footage can be seen in Figure 3.7, and the tracked trajectories can be seen in Figure 3.8. In the beginning near $t = 0$, the expansion of the particles is clearly resolved. However, since the system is fixed-boundary, the wave propagation started to bounce back and forth in the system - a phenomenon similar to reflection waves. It can also be seen that the motion of the particles begin to die out at the time goes on. Unfortunately, friction is not 100% eliminated and contributed to the diminishing of the particle motion. However, the

3.2 Particle Trajectories

tracking time for this experiment is long ($t_{total} = 4\text{s}$), which is arguably too lengthy. Much of the information can be extracted from just the first second of the simulation.

Also notable is that in Caplan et al.'s (2012) report, the pre-compression test case was also conducted. However, no result was obtained due to sub-optimal lighting and the tracking program's inability to pick up the motion of the particles. The existence of friction also reduced the visibility of the expansion wave. This indicates that better lighting, reduced friction, and more robust tracking code dramatically improved the device overall, leading to experimental results unobtainable before.

Chapter 4

Modelling

Since the magnet chain was designed to be free-interacting, their trajectories can almost be intuitively predicted. However, a better way to predict the trajectories was needed. The objective was develop a numerical simulator (using MATLAB) that is modelled after the physical system. To that end, the equations of motion for each particle needed to be developed, which relied on the magnetic force potential between the magnets. To obtain the force potential, various avenues were explored in the quest to obtain the most accurate interaction forces.

4.1 Numerical Simulation

One-dimensional chains of discrete particles are traditional systems (Fermi et al., 1955; Nesterenko, 1983) to obtain physically based partial differential wave equations. However, various approximations need to made for the wave equations to be valid (Nesterenko, 2001, p.105). Since it is possible to numerically simulate the system directly without using approximations, the wave equations would be abandoned in favour of general equations of motion.

Modelling

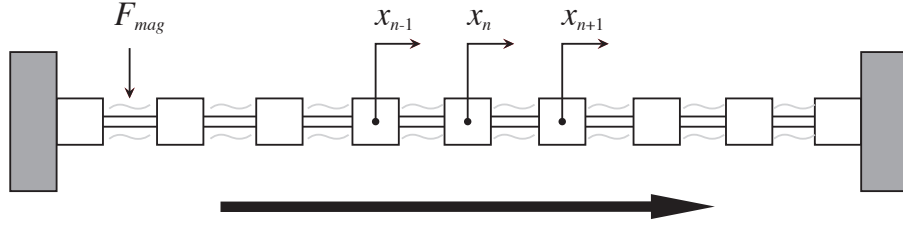


Fig. 4.1 The simulator uses this analogy. F_{mag} is the repulsive magnetic force acting between two neighbouring magnets. The particles' coordinates are indicated with by x_n . The two magnets on the ends of the chain are fixed to the boundary. The arrow at the bottom shows the direction of positive x .

The system of equations for a discrete chain of particles interacting according to general law only to the closest neighbours can be derived by applying Newton's Second Law to each individual magnet depicted in Figure 4.1:

$$m\ddot{x}_i = F_{net} = F_{mag}(x_{i-1} - x_i) - F_{mag}(x_i - x_{i+1}). \quad (4.1)$$

Also it is given by Nesterenko (1995):

$$m\ddot{x}_i = F_{mag}(x_{i-1} - x_i) - F_{mag}(x_i - x_{i+1}), \quad N \geq i \geq 2, \quad (4.2)$$

where m is the mass of the magnets, $F_{mag}(x_i - x_i)$ is the magnetic interactive force between them with numbers i , x_i is the displacement of the i th magnet from the leftmost magnet, and N is the number of magnets in the system, including the two fixed on the ends.

With this, a MATLAB numerical simulator could be developed. MATLAB has an internal differential equation integrator in `ode45`, which uses a four-stage Runge-Kutta scheme to obtain the solution in a time-step fashion. It is also able to solve any arbitrary number of equations, which is helpful because each individual particle requires one equation of motion. Thus, for

N particles, the simulator must solve for N equations simultaneously. An overview of the numerical simulator is as follows:

1. Define parameters of the system: total length, mass of the magnets, dimensions of the magnets, total time, and sampling rate
2. Define initial positions and velocities and different test schemes
3. Use `ode45` to integrate the N equations of motion to obtain the particle trajectories
4. Perform post-processing on the trajectories to for animation, wave finding, etc

It is clear, at this point, that an accurate numerical representation for $F_{mag}(x)$ is needed to determine the amount of force between the magnets for any given separation.

4.1.1 Magnetic Force Potential

Analytical Solution

In a recent paper, Vokoun et al. (2009) developed an analytical expression for the magneto-static force between two cylindrical magnets (radius R , thickness $t_i, i = 1, 2$, and saturation magnetization M) with a common axis separated by Z (centre-to-centre), and it is given by

$$F_z = -8\pi K_d R^2 \int_0^{+\infty} \frac{J_1^2(q)}{q} \sinh(q\tau_1) \sinh(q\tau_2) e^{-q\zeta} dq, \quad (4.3)$$

where $K_d = \mu_0 M^2 / 2$, μ_0 is the vacuum permeability, $J_1(q)$ is a modified Bessel function, $\tau_i = t_i / (2R), i = 1, 2$, are the aspect ratios of the two cylinder, $\zeta = Z/R$ is the reduced distance between the centres of the two cylinders. After rewriting the hyperbolic function in terms of exponentials, the integral in 4.3 can be written in terms of combination of elliptical inte-

Modelling

grals $A_{11}^0(\omega, 1, 1)$ as described by Eason et al. (1955); Prudnikov et al. (1986) since it is of Lipschitz–Hankel type:

$$F_z = -2\pi K_d R^2 \sum_{i,j=-1}^1 i \cdot j \cdot A_{11}^0(\zeta + i\tau_1 + j\tau_2, 1, 1), \quad (4.4)$$

where

$$A_{11}^0(\omega, 1, 1) = \frac{\omega}{\pi k_1} E(k_1^2) - \frac{(2 + 0.5\omega^2)k_1\omega}{2\pi} K(k_1^2) + \frac{1}{2}, \quad (4.5)$$

$k_1^2 = 4/(4 + \omega^2)$, and K and E are complete elliptic integrals of the first and the second kind, respectively (Prudnikov et al., 1986).

Furthermore, Vokoun et al. determined that if the cylindrical magnets are far from each other, $t_1 = t_2 = t$, using $\zeta = (2t)/(2R) + x/R$, where x is the gap between the magnets, it is possible to obtain

$$F_z \approx -\frac{1}{2}\pi K_d R^4 \left[\frac{1}{x^2} + \frac{1}{(x+2t)^2} - \frac{2}{(x+t)^2} \right]. \quad (4.6)$$

Equation 4.6 gives the approximate force between two *distant*, identical cylindrical magnets magnetized along a common axis. However, Equation 4.6 gives an erroneous approximation for small separations between the magnets as the force values approach infinite for close-to-zero gap, and as the Vokoun et al. put it, “this approximation corresponds to the situation when the cylindrical magnets are replaced by dipoles, and is of very limited validity.” Its validity in the subject study will be further verified at the end of this section.

Equation 4.6 is invalid for small separation of magnets; Equation 4.3 cannot be readily computed without the use of elliptic integrals, its usage was considered out of scope for this study. Hence, an alternative method of obtaining a numerical expression for the force between the magnets.

Table 4.1 Dynamic loading test cases

Test	Initial Velocity (m/s)	Frames per Second
1	3.3662	3000
2	3.5801	3000
3	3.1864	5000
4	3.4295	5000
5	3.4639	5000
6	5.1940	5000
7	3.0911	9300
8	4.1644	9300
9	5.0063	9300

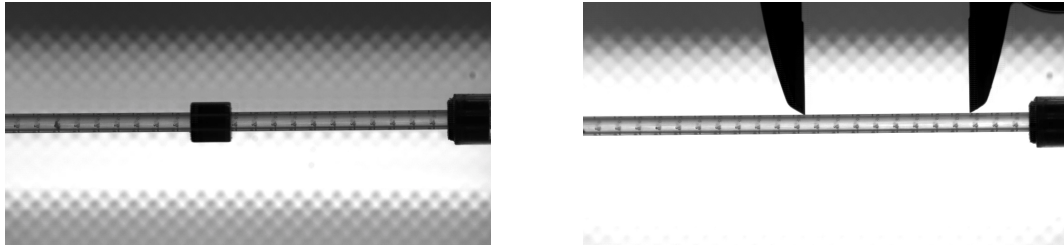


Fig. 4.2 Very high-speed photography (9300 FPS) was used to obtain the trajectory of one magnet as it is launched towards another magnet positioned in a repulsive orientation

Dynamic Loading

With the MATLAB particle tracking tool developed (see Chapter 3), it became possible to use high-speed photography to capture the dynamics of a magnet as it approaches another magnet. That is, since the force between magnets stays constant regardless of how fast they travel with respect to each other, it is possible to “launch” a magnet towards another at varying speeds and obtain varying trajectories. Faster the initial velocity, the closer the magnets would approach, which can provide information of the magnetic force at that given gap.

The trajectory information enables the finding of the magnetic force profile over time by taking the second time derivative of the position vector. Since the displacement interval is

Modelling

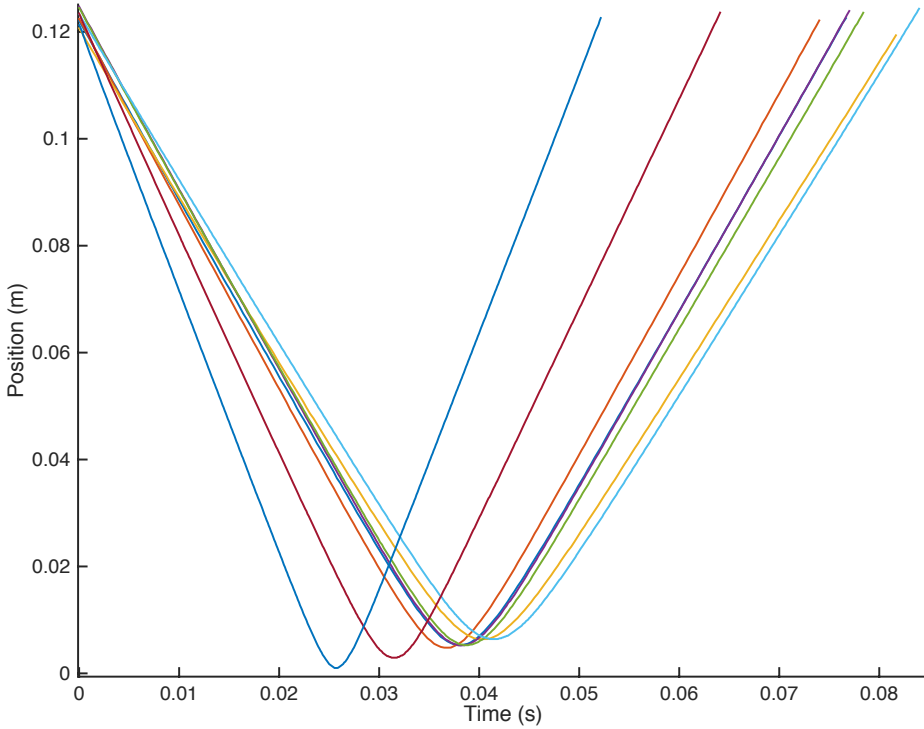


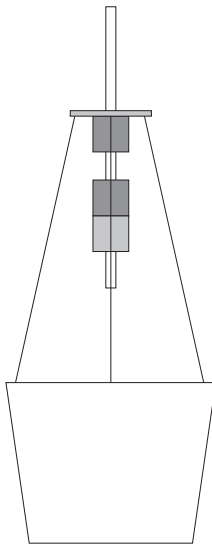
Fig. 4.3 The trajectories of the dynamic loading test cases as tracked and recreated by MATLAB

well-resolved (a ruler was used for scale, see Figure 4.2), the profile can be used to deduce the magnetic force over given displacement.

A total of nine tests were performed for varying frame rates and initial velocities. The incoming magnet was launched by hand using a rod. The air bearing system was turned on to decrease the effect of friction. The test specifications can be found in Table 4.1, and the resulting trajectories can be seen in Figure 4.3. The resulting force over displacement data points can be seen in Figure 4.5. The data collected is not included in this report for brevity.

Static Loading

In order to obtain more concrete data points for smaller separations ($x < t_{mag}$), some static loading test cases were proposed. Essentially, the process is as follows:



(a) Diagram of the experimental apparatus



(b) Photo of the experimental apparatus

Fig. 4.4 Setup for the static loading test cases. The hanging pan at the bottom allows for loads to be evenly distributed onto the top magnet.

1. Place the two magnets with the same poles facing each other, so that they repel each other
2. Measure the separation between the magnets
3. Since the weight of the magnets is known, the relationship between load and separation can be obtained
4. Continue to load more weight on the top magnet, and measure the separation each time
5. Obtain the overall relationship between load/force and separation

There are some challenges to setting up this experiment. Since the magnetic force relations are desired, anything ferrous material would undoubtedly distort the results because the magnets would be attracted to it. Also, uniformly loading large amount of weight onto the top magnet, without the weights resting against the centre rod, would be difficult. Lastly, accurate and

Modelling

precise measurements of the separation between the magnets could be challenging, and made especially so because no ferrous material (i.e. steel) could be used.

To combat these challenges, an experimental apparatus depicted in Figure 4.4 was constructed. This apparatus was designed to be hanged from above, which helps the device to stay strictly vertical even with additional weights. The hanging pan below is attached to an aluminium plate that rests on top the top magnet via some strings, and brass weights can be loaded into them. The separation between the magnets is measured using digital photography.

The results of the static loading are direct representations of the magnetic force potential, and no numerical derivatives need to be taken. Fortunately, the results of this experiment aligned well with those obtained via dynamic loading. The results can be seen in Figure 4.5. The data collected can be found in Appendix A.

Force Potential Result

The results from dynamic loading and static loading were processed and translated to force v.s. separation (face-to-face). A MATLAB curve-fitting algorithm was used to determine the appropriate numerical expression for the force potential. Although the ring magnets are not simple dipoles, it was speculated that they still interact with each other in ways similar to the inverse-square law. Also, because the force potential is defined by face-to-face separation (centre-to-centre data is not obtainable because it is not possible to have magnets physically overlap each other), the contact force is a finite value. Therefore, it was theorized that the force potential is of the form

$$F_{mag}(x) = A(x + C)^B, \quad (4.7)$$

4.1 Numerical Simulation

where A , B , and C are unknown coefficients to be determined by the curve-fitting algorithm. Since the data from dynamic loading can be noisy due to the fact that it was obtained by taking the second time derivative of the particle trajectories, a bi-square fitting scheme was used to lower the weight of the outliers. From there, the MATLAB algorithm produced the expression with $R^2 = 0.9818$ was found as

$$F_{mag}(x) = 0.0003020(x + 0.0049398)^{-2.2274940}, \quad (4.8)$$

where $F_{mag}(x)$, measured in newtons, is the magnetic repulsive force as a function of magnet face-to-face separation x , measured in metres. The results are promising: at $x = 0$ m, the force is $F_{mag}(0) = 41.4$ N, which aligns well with the vendor's data (K&J Magnetics, 2008).

Equation 4.8 was used in the MATLAB numerical simulator. The analytical solution in Equation 4.6 is plotted with the final force curve in Figure 4.5. It can be concluded that the empirical results are much better than the analytical approximation. Finally, the numerical simulation results, generated using Equation 4.8, can be found in Section 4.1.2.

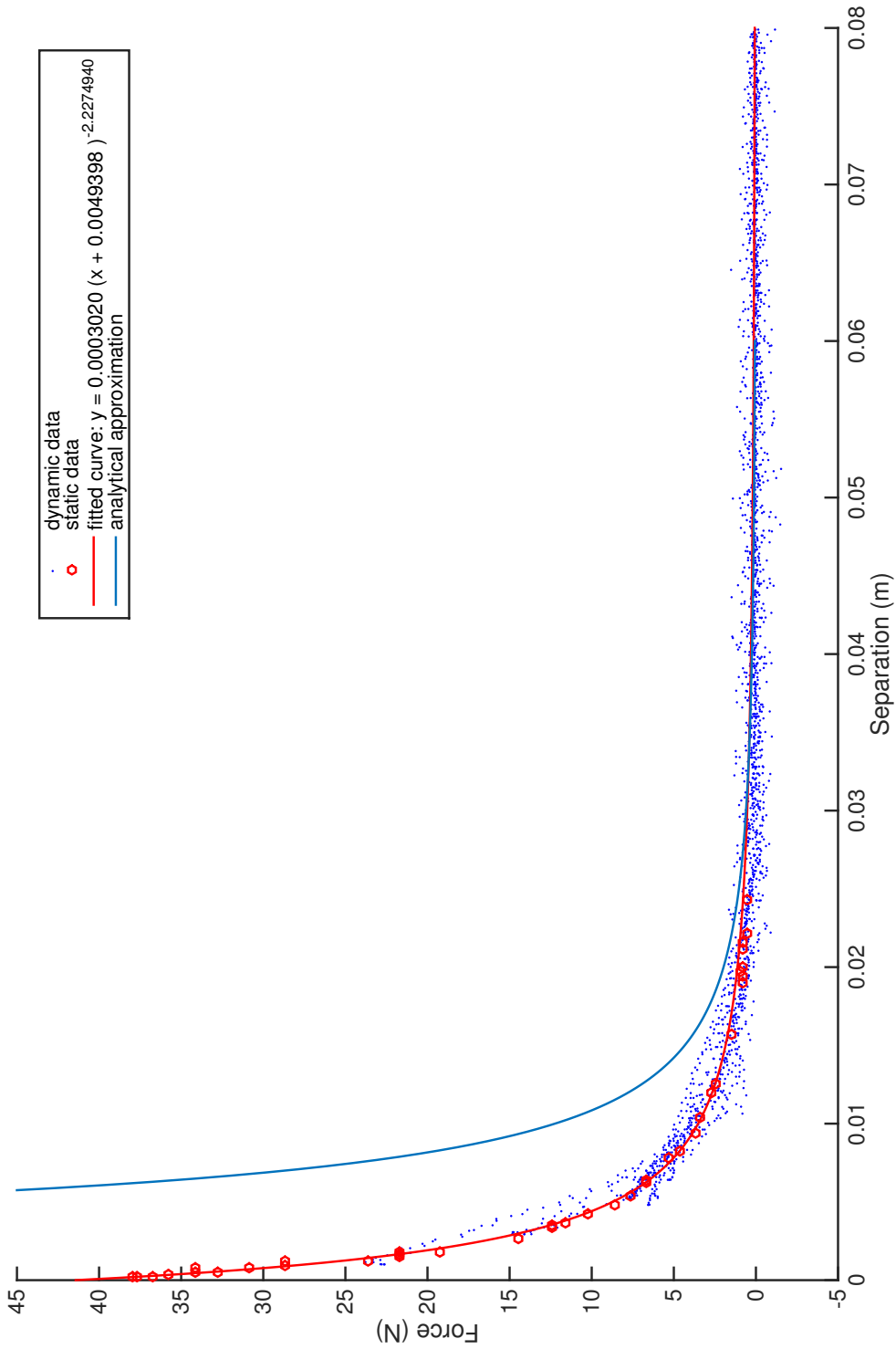


Fig. 4.5 The magnetic force potential for given separation (face to face) of magnets. The blue dots are results from dynamic loading, the red circles are results from static loading, the red curve is the fitted curve using MATLAB's curve-fitting algorithm, and the blue curve is the analytical solution using Equation 4.6

4.1.2 Numerical Simulation Results

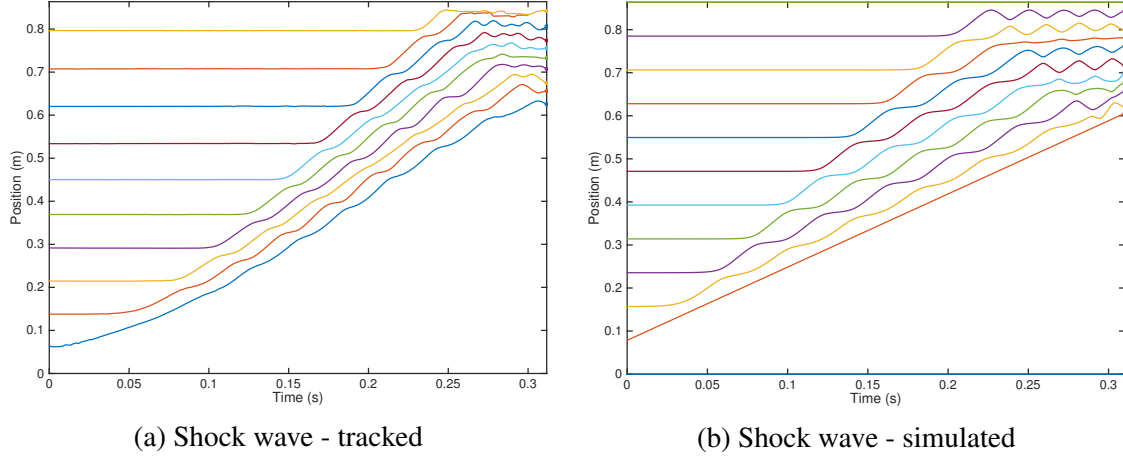


Fig. 4.6 Shock wave test case: reality vs simulation

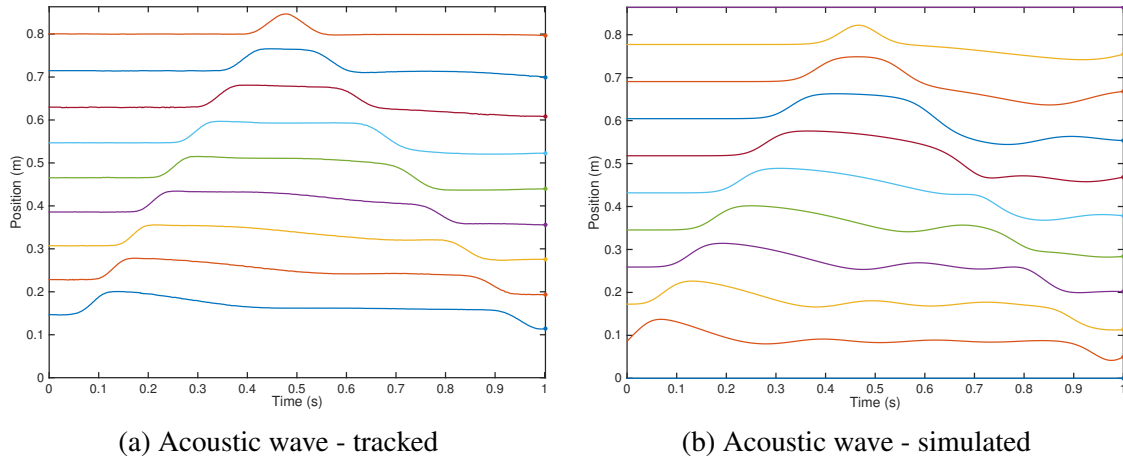


Fig. 4.7 Acoustic wave test case: reality vs simulation

Figure 4.6, 4.7, and 4.8 show the three test cases in tracked and simulated scenarios. For all tests, all the physical parameters were aligned to the best of ability. It is easy to see that for the shock and acoustic wave the tracked trajectories qualitatively match the simulated trajectories, but quantitatively there is significant difference. For the expansion wave/pre-compression test case, however, the tracked and simulated results match up well.

Modelling

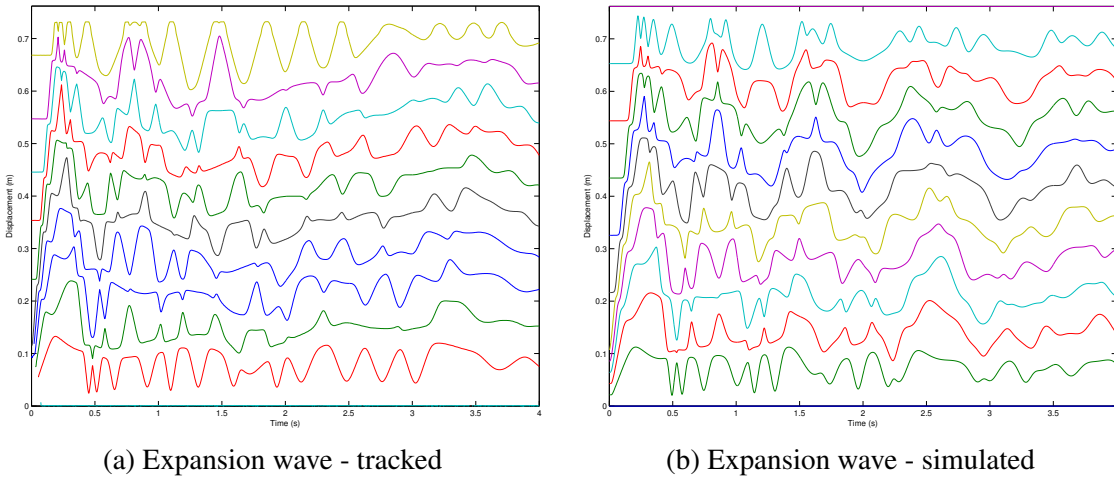


Fig. 4.8 Expansion wave test case: reality vs simulation

This can be explained. For the shock and acoustic wave, the inputs to the system were initiated by hand. For the simulated scenario, the inputs were defined by an initial condition input.

For the shock wave case, the first particle was maintained at a constant velocity. In the simulation, this velocity stays perfectly constant. However, in reality the same cannot be easily achieved, and, as seen in the plot, the driving piston's velocity varied.

For the acoustic wave case, the first particle was given a velocity initial condition. However, in reality the input is more similar to an impulse input than an initial velocity condition input. It is not possible to simulate the hand input, and therefore impossible to obtain the exact same output.

Lastly, the outputs are similar for the pre-compression case because the inputs are well-defined both in simulation and in reality. In simulation, the input can be defined as initial position conditions. In reality, the clamp arms hold the magnets in place - just like initial position conditions. This explains the similarity.

Consequently, in order to have simulation better match reality, better input methods should be developed for acoustic and shock wave test cases. A mechanical or electromagnetic actuator

seems to be ideal for the task (see Section 5.1), but the design and fabrication of this device is out of scope for this study.

4.2 Analytical Continuum Modelling

The main objective of the study was to see if it were possible to conceive an experimental apparatus that could simulate wave dynamics and propagation in different types of regimes. As discussed in Chapter 1, it could be possible to make this mechanical analogue using magnets as particles. As the particles are spaced further apart, their dynamics can almost be approximated by beads-on-wire collision events (Higgins, 2011). In this regime, the pulse velocity in the chain would simply approach the initial velocity of the collision, as particles interact with each other almost exactly like elastic collisions, or billiard balls. As they come closer together, but not too close, the nonlinearity in the force potential begins to play a major part in the wave velocity. In this regime, the pulse velocity can no longer be analysed with simple collision events. The pulse velocity becomes a combination of the translational speeds of the particles *and* the strength of the potential between them. This analysis remains a challenge (Rosas and Lindenberg, 2004). Lastly, if the magnets are spaced tightly, their dynamics become similar to an ideal gas like media at a macroscopic scale - continuous or Hooke's Law media. The pulse velocity in this regime should be relatively easy to analyse, and the result is well known (Huggins, 2008).

For very small particle separation, the motion of the magnets become *restricted*. Because the force potential becomes so strong once the magnets move out of equilibrium, motions of the magnets become small perturbations about their equilibrium positions. If Taylor series expansion was done for each magnet about the equilibrium positions, one is left with simple linear terms after the higher order terms are eliminated. This process of linearisation can lead to

Modelling

a continuous approximation of the one-dimensional chain with good results (Nesterenko, 1995).

In this continuous approximation, a disturbance would create a pulse that would propagate through the system at a defined velocity: the sound speed. It is given by Equation 1.9, reproduced here:

$$v_{pulse} = \sqrt{\frac{K_{total}L}{\mu}},$$

where K_{total} is the total spring constant¹, L is the length of the chain, and μ is the effective density of the chain, given by $\mu = M/L$.

Thus, if the one-dimensional chain in the subject study can be modified such that the initial separation between the magnets become small enough so any disturbance in the system could only cause small perturbations, the system should show resistance to increasing amount of energy input. That is, for different energy inputs in the form of initial velocities, when the system is “dense”, the responses should converge. It is expected to see only one pulse velocity for a given density - effectively, initial separation - and it is given by Equation 1.9².

A simulation in MATLAB was performed to validate this hypothesis. The same simulator was used to perform these tests. For the energy input, one of the magnets was given an initial velocity. With that, more and more magnets were added into the system, which decreased the separation between each one. For each instance of particle addition, the resulting trajectories were determined with `ode45`, and a wave-finding scheme was used to determine the velocity at which the pulse propagated in the one-dimensional system. Each set of trajectories resulted in one data point. Once the program found the wave speed for very small separations, a higher energy input was specified (higher initial velocity), and the same process repeated.

¹which is equal to the reciprocal of the sum of the reciprocals of all the individual spring constants K_i , or $1/K_{total} = \sum_{i=1}^N 1/K_i$

²Here, the spring constant is the instantaneous slope of the force potential for the given separation, and can be obtained by taking the derivative of the force with respect to separation

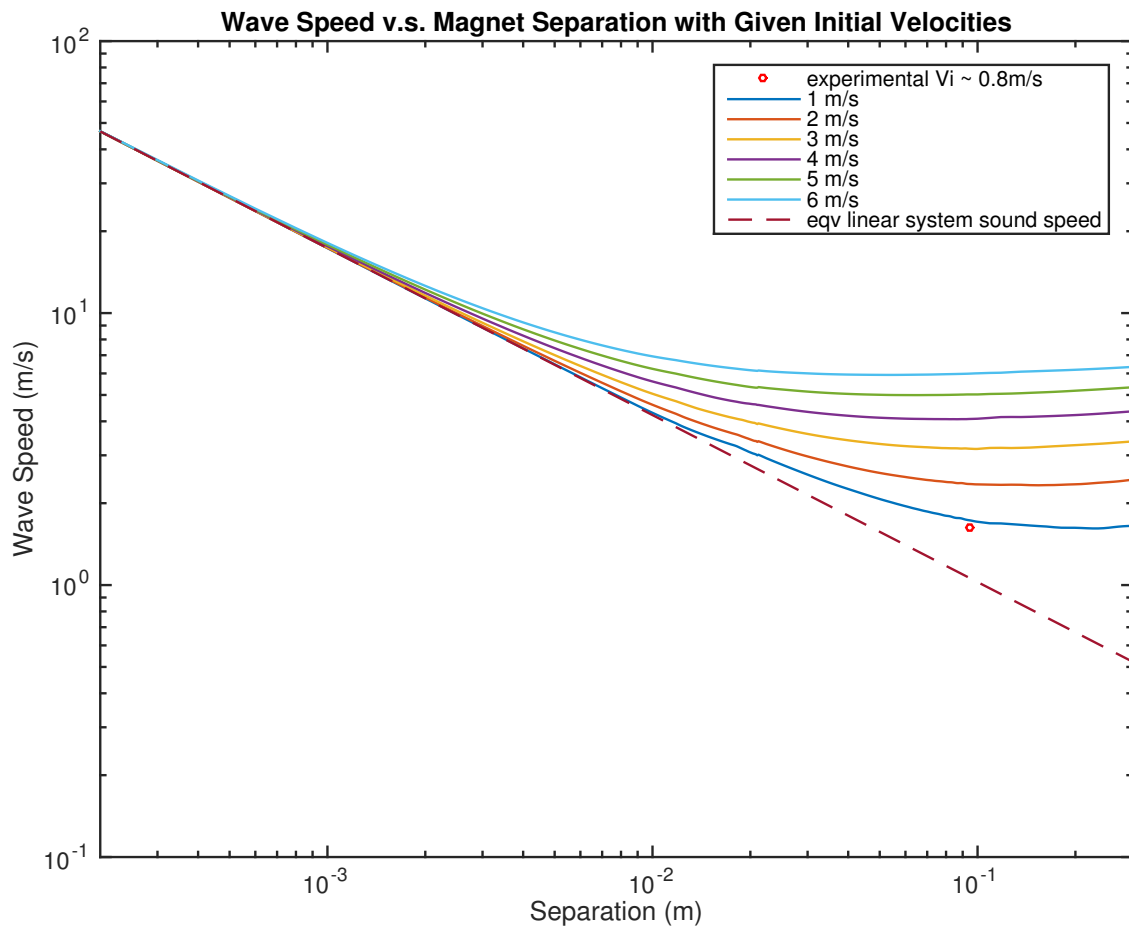


Fig. 4.9 Plot of the speed of detected wave propagation v.s. magnet separation for given initial velocities. As the magnets get closer and closer together, the one-dimensional chain begin to behave like continuous material with defined a sound speed.

Modelling

Figure 4.9 shows the resulting pulse velocity profile. As expected, the various energy inputs have no impact to pulse velocity at high density/small separation. In fact, they converged onto the equivalent linear system, suggesting that for small separations, the system's dynamics can be well-approximated with linear methods. However, as the gaps widen, the system begins to diverge from linear system behaviour. This shows that the one-dimensional magnetic chain can be used to observe wave propagation in both linear and nonlinear regimes.

On the same graph, only one experimental data point can be seen. However, it seemed to conform to the simulated ideals. In order to validate the physical apparatus for the same continuum model, more data points need to be gathered. However, some challenges must be overcome for this to become a reality. See Section 5.1 for future work.

Chapter 5

Conclusion

The mechanics of wave propagation are different in different media and regimes. Three different regimes were investigated: bead-on-a-wire, nonlinear/granular, and linear/continuous. It was hypothesized that a one-dimensional chain of magnets, if can be made to interact freely, could be used to observe wave propagation in different regimes. Such a system could serve to be a convenient mechanical analogue for particular interaction in general, switching to different regimes via the addition and elimination of magnets.

A physical, one-dimensional chain of magnets was constructed. In order to have free magnetic interaction, a way to eliminate friction and the effect of gravity was needed. An air bearing system with laser-drilled acrylic tube was fabricated, which allowed the horizontal orientation of the one-dimensional magnetic chain. Consequently, the effects of friction and gravity were appreciably minimized.

A system to capture high-speed photography and analyse results using computerized particle tracking was also developed. It was shown that, with the help of open-source particle tracking algorithm, a MATLAB-based computer program can reliably extract trajectories from video footage.

Conclusion

A MATLAB numerical simulator modelled after the physical system showed good agreement between simulation and reality. This indicated that the minimization of the effects of gravity and friction significantly eased the process of validating the physical system. In order for the numerical simulator to be accurate, empirical methods were used to obtain the repulsive magnetic force potential to good effect. Static loading and dynamic methods were used, and a curve-fitting algorithm produced the numerical expression for the force potential.

Simulations were performed and showed that, theoretically, the system could be used to observe wave propagation in different regimes. For high density of magnets, the system exhibits behaviour similar to that seen in continuous media. For low density of magnets, the system was seen to behave with undefined sound speeds, and, eventually, beads-on-a-wire wave propagation. However, not enough experimental data was obtained to verify the same theory for the physical magnetic chain.

5.1 Future Work

In general, more experimental data need to be gathered to fully realize the objectives of the physical one-dimensional magnetic chain. To do that, the device should be improved.

In order to verify the continuum modelling of the system, a large number of magnets need to be added. However, given that the additional load would be added onto the acrylic air bearing tube, concerns of structural integrity were raised. Acrylic is not rigid enough for the large addition of magnets, and the chain no longer stays straight with the increased load. The sagging of the acrylic tube is problematic in that 1) it changes the dynamics of the magnets by introducing changes in gravitational potential energy, and 2) it might cause the tube to break (expensive to replace). To that end, different materials for the air bearing tube should be investigated. One candidate is ceramic, which should provide better rigidity.

5.1 Future Work

For the simulations to better match reality, ways to improve energy input should be explored. As of now, energy input is initiated by hand, which is inconsistent and unrepeatable, especially in simulation. A better way would be to utilize electromagnetic actuators that can consistently generate impulse inputs into the system. The design and manufacturing of such a device must take in to account that the dynamics of moving magnets adjacent to it must remain undisturbed, i.e. the use conductive material should be minimized.

Other future work might include making the software tools used faster, more standalone, and more user-friendly. However, the main focus should be to improve the experimental apparatus so that more data can be gathered.

References

- Blair, D. and Dufresne, E. (2008). The Matlab Particle Tracking Code Repository. <http://site.physics.georgetown.edu/matlab/>. Accessed: 2014-04-20.
- Caplan, P., LeBlanc, D., Sirignano, A., and Star, A. (2012). One-Dimensional Shock and Detonation Wave Simulator. Technical report, McGill University Mechanical Engineering Project.
- Coulomb, C. (1785). Premier mémoire sur l. *Électricité et le Magnétisme*'Mém. Acad. R. Sci, 88:569.
- Crocker, J. C. and Grier, D. G. (1996). Methods of digital video microscopy for colloidal studies. *Journal of colloid and interface science*, 179(1):298–310.
- Crocker, J. C. and Grier, D. G. (2008). Particle tracking using IDL. <http://www.physics.emory.edu/faculty/weeks//idl/>. Accessed: 2014-05-03.
- Eason, G., Noble, B., and Sneddon, I. N. (1955). On Certain Integrals of Lipschitz-Hankel Type Involving Products of Bessel Functions. *Philosophical Transactions of the Royal Society of London A: Mathematical, Physical and Engineering Sciences*, 247(935):529–551.
- Fermi, E., Pasta, J., and Ulam, S. (1955). Studies of nonlinear problems.
- Higgins, A. (2011). Shock-like and Detonation-like Waves in One-dimensional Lattice Chains. In *23rd International Colloquium on the Dynamics of Explosions and Reactive Systems*, Irvine, CA.
- Huggins, E. (2008). Speed of wave pulses in Hooke's law media. *The Physics Teacher*, 46(3):142–146.
- K&J Magnetics, I. (2008). R848 Ring Magnet Specifications. <http://www.kjmagnetics.com/proddetail.asp?prod=R848>. Accessed: 2014-05-02.
- Landau, L. D. and Lifshitz, E. M. (1959). *Course of Theoretical Physics Vol 7: Theory and Elasticity*. Pergamon Press.
- Nesterenko, V. F. (1983). Propagation of nonlinear compression pulses in granular media. *Journal of Applied Mechanics and Technical Physics*, 24(5):733–743.

References

- Nesterenko, V. F. (1995). Continuous approximation for wave perturbations in a nonlinear discrete medium. *Combustion, Explosion and Shock Waves*, 31(1):116–119.
- Nesterenko, V. F. (2001). *Dynamics of heterogeneous materials*. Springer.
- Prudnikov, A. P., Brychkov, I. A., and Marichev, O. I. (1986). *Integrals and series: special functions*, volume 2. CRC Press.
- Rosas, A. and Lindenberg, K. (2004). Pulse velocity in a granular chain. *Physical Review E*, 69(3):037601.
- Vokoun, D., Beleggia, M., Heller, L., and Šittner, P. (2009). Magnetostatic interactions and forces between cylindrical permanent magnets. *Journal of Magnetism and Magnetic Materials*, 321(22):3758–3763.
- Wu, D. T. (2002). Conservation principles in solitary impulse propagation through granular chains. *Physica A: Statistical Mechanics and its Applications*, 315(1):194–202.

Appendix A

Raw Data From Static Loading

Table A.1 Set 1

Point	Mass (g)	Disp (px)	Disp (m)	Force (N)
1	75.4	103	0.0210944	0.739674
2	95.4	96	0.0196608	0.935874
3	145.4	77	0.0157696	1.426374
4	245.4	61	0.0124928	2.407374
5	345.4	51	0.0104448	3.388374
6	545.4	38.5	0.0078848	5.350374
7	1045.4	21	0.0043008	10.255374
8	676.3	31	0.0063488	6.634503
9	1268.2	17	0.0034816	12.441042
10	2207.8	9	0.0018432	21.658518
11	2925.1	6	0.0012288	28.695231
12	3475.2	4	0.0008192	34.091712

Raw Data From Static Loading

Table A.2 Set 2

Point	Mass (g)	Disp (px)	Disp (m)	Force (N)
1	48.9	85	0.024330203803	0.479709
2	58.9	77.5	0.0221834211145	0.577809
3	78.9	70	0.020036638426	0.774009
4	83.9	68	0.0194641630424	0.823059
5	85.9	66.5	0.0190348065047	0.842679

Table A.3 Set 3

Point	Mass (g)	Disp (px)	Disp (m)	Force (N)
1	3475.2	10.5	0.000504	34.091712
2	2925.1	18.5	0.000888	28.695231
3	2207.7	33.5	0.001608	21.657537
4	3146.5	15	0.00072	30.867165
5	3863.7	5	0.00024	37.902897
6	3646.4	7.5	0.00036	35.771184
7	3346.4	11	0.000528	32.828184
8	3846.4	4.5	0.000216	37.733184
9	3746.4	5	0.00024	36.752184
11	2207.5	30	0.00144	21.655575
12	2407.5	25.5	0.001224	23.617575
13	1267.9	69	0.003312	12.438099
14	1467.9	55	0.00264	14.400099
15	1967.9	37.5	0.0018	19.305099
16	676	130.5	0.006264	6.63156
17	876	100	0.0048	8.59356
18	1176	76	0.003648	11.53656
19	776	113.5	0.005448	7.61256
20	275.4	248.5	0.011928	2.701674
21	375.4	194.5	0.009336	3.682674
22	475.4	171	0.008208	4.663674
23	75.4	451	0.021648	0.739674